*J. Fluid Mech.* (1985), *vol.* 152, *pp.* 391–418
*Printed in Great Britain*

# Nonlinear Rayleigh-Bénard convection with square planform

By WAYNE ARTER†

Department of Applied Mathematics and Theoretical Physics,
Silver Street, Cambridge, CB3 9EW

(Received 7 July 1983 and in revised form 12 October 1984)

Fully three-dimensional numerical solutions are presented for Rayleigh–Bénard convection subject to stress-free boundary conditions. A motion with square planform is studied for varying Rayleigh number $R$ and Prandtl number $\sigma$. It may be understood partly in terms of a truncated modal representation (after Lorenz 1963). Thermal layers of unusual structure are found at high $R$. For small $\sigma$, steady solutions exist, but are not of 'flywheel' type, and the heat transport depends strongly on $\sigma$. The study also verifies that laminar convective flows may be ergodic.

## 1. Introduction

The Rayleigh–Bénard problem concerns a layer of Boussinesq fluid confined between horizontal boundaries and heated from below (see e.g. Chandrasekhar 1961). It has been, and continues to be, subject to intense study because of its widespread application and many fascinating aspects (Busse 1978). We remark that the simplest theoretical idealization of infinite layer and 'stress-free' boundary conditions is distinct from the usual laboratory experiment which involves a fluid bounded by fixed plates on all sides. We take the theoretician's viewpoint, content with an indirect approach to both laboratory and astrophysical convection.

The latter flows lack rigid boundaries, but are normally turbulent, taking the form of cells rather than rolls. However, even when the motion is two-dimensional or nearly so, it is not easy to predict the exact wavelength that is preferred (Jhaveri & Homsy 1980). In the laboratory, the lateral boundaries even in containers of very large horizontal extent make things more complicated: in particular the flow may become irregularly time-dependent even at the onset of convection (Ahlers & Behringer 1978). Much theoretical progress has been made (Zippelius & Siggia 1982; Cross 1982, 1983; Cross *et al.* 1983; Greenside, Coughran & Schryer 1982), but it is difficult to see how to relate this work closely to e.g. a stellar convection zone. We follow Moore & Weiss (1973, hereinafter referred to as MW) by selecting a planform, and then subjecting it to thorough investigation.

We choose the square planform, even though in an extended layer with perfectly thermally conducting boundaries, it is known to be unstable on theoretical grounds in both the viscous (Schlüter, Lortz & Busse 1965) and inviscid (§2.3) limits. However, Schlüter *et al.* also show that motions with hexagonal planform are unstable, and bimodal convection is known to occur only over a narrow range of parameters (Busse 1978). Square cells are readily accessible to analytic and numerical

---

† Present address: Culham Laboratory, Abingdon, Oxon, OX14 3DB (UKAEA/Euratom Fusion Association).

investigation, and the contrast with the results of Jones, Moore & Weiss (1976, hereinafter referred to as JMW) for axisymmetric convection should be particularly interesting. Moreover, Jenkins & Proctor (1984) have predicted that the square planform should be preferred when poorly conducting boundaries are used, although they did not consider bimodal flows.

Further caution is necessary, because linear theory predicts a motion with square planform consisting of two sets of rolls intersecting each other at right angles, which does not accord with solar observations: regions of rising fluid are surrounded by ones where flow is downward, a property of the hexagonal cell (Stuart 1964). In §2 we consider second-order theory, which predicts a flow with the same topological properties as does linear theory. In addition we derive for the time-dependent problem a truncated modal representation (after Lorenz 1963), which for moderate values of $R$, although it exhibits some interesting transient phenomena, apparently has asymptotically only steady solutions. These show unphysical behaviour at quite small $R$ (cf. Malkus & Veronis 1958), so for larger $R$ we proceed to a numerical investigation of the governing equations.

There have been several computations using fixed-plate boundary conditions for these $R$, motivated by the experiments of notably Krishnamurti (1970, 1973). She and others typically found, as reviewed by Busse (1978), that convection at onset takes the form of rolls, becomes three-dimensional at higher $R$ and finally turbulent. Fully three-dimensional calculations are still very expensive to perform. The early investigations (Lipps & Somerville 1971; Veltishchev & Zelnin 1975; Ozoe *et al.* 1976) all suffer in varying degrees from lack of computer store and time, while Lipps (1976) and Grötzbach (1982) study only a few parameter values and have chiefly been concerned with transitions in the convective planform. Our aim has been to follow less obvious but nonetheless important changes in the flow properties with greater resolution in $(R, \sigma)$-space. We describe the necessary computational techniques in §3 and present numerical results for the ranges $1500 \leqslant R \leqslant 60000$ ($\sigma = 1$) and $0.035 \leqslant \sigma \leqslant 10$ ($R = 5000$) in §§4 and 5. Subsection 5.3 contains other calculations at low $\sigma$. We consider the stability of these solutions and the effect of changing initial conditions in §6.

The three-dimensional flows found are related to the bimodal and square-cell convection found in laboratory experiments (Busse 1978; Frick, Busse & Clever 1983). Our high-$\sigma$ results may be understood in terms of the simple boundary-layer model described by MW, but 'flywheel' convection is not found at low Prandtl number. Instead we discover that in most respects decreasing $\sigma < 1$ at constant $R$ corresponds to increasing $R$ at $\sigma = 1$. We confirm that the flow in these two régimes, when the Reynolds number is large, becomes ergodic as predicted by Arter (1983*b*). The asymptotic scalings are not well-determined, but it seems that Nusselt number $N \propto R^{0.3}$ as $R \rightarrow \infty$ for $\sigma = 1$, and $N$ depends strongly on $\sigma$ as $\sigma \rightarrow 0$ at fixed $R$. For further discussion see the concluding §7.

## 2. Analytic results

### 2.1. *Statement of the problem and linear theory*

The governing equations are given by Chandrasekhar (1961). Let $T$ be temperature, $\boldsymbol{u}$ the velocity, $\boldsymbol{\omega} = \operatorname{curl} \boldsymbol{u}$ the vorticity and $p$ the pressure field. In the Boussinesq approximation, the momentum equation is

$$\frac{\partial \boldsymbol{u}}{\partial t} = -(\boldsymbol{u} \cdot \operatorname{grad}) \boldsymbol{u} - \frac{1}{\rho_0} \operatorname{grad} p + \frac{\rho - \rho_r}{\rho_0} \boldsymbol{g} + \nu \nabla^2 \boldsymbol{u}, \qquad (2.1a)$$

subject to $\operatorname{div}\boldsymbol{u} = 0$, where density $\rho = \rho_0[1-\alpha(T-T_0)]$. $T$ satisfies

$$\frac{\partial T}{\partial t} = -\boldsymbol{u}\cdot\operatorname{grad} T + \kappa\nabla^2 T. \tag{2.1$b$}$$

$\kappa$ and $\nu$ are the thermal and viscous diffusivities, $\rho_{\mathrm{r}}$ is a reference density distribution and gravity $\boldsymbol{g}$ acts in the negative $z$-direction ($\boldsymbol{g} = -g\hat{\boldsymbol{z}}$, $g > 0$). We also consider the vorticity equation, which follows from the momentum equation, and is

$$\frac{\partial \boldsymbol{\omega}}{\partial t} = \operatorname{curl}(\boldsymbol{u}\times\boldsymbol{\omega}) + \frac{1}{\rho_0}\operatorname{grad}\rho\times\boldsymbol{g} + \nu\nabla^2\boldsymbol{\omega}. \tag{2.2}$$

The form of $\rho_{\mathrm{r}}$ is chosen by taking the corresponding temperature distribution to be

$$T_{\mathrm{r}}(z) = T_0 + \Delta T(1-z),$$

where $\Delta T$ is the temperature difference across the layer of fluid. The set of equations may be made dimensionless by scaling distance with layer depth $d$ and $t$ with respect to the thermal diffusion time $d^2\kappa^{-1}$. This introduces Rayleigh number $R = g\alpha\,\Delta T\, d^3/\kappa\nu$ and Prandtl number $\sigma = \nu/\kappa$.

Boundary conditions for $\boldsymbol{u}$ and $T$ are given by Chandrasekhar (1961). Normal $\boldsymbol{u}$ is taken to vanish on the faces of a $\lambda\times\Lambda\times 1$ box with stress-free boundaries. The box has its upper and lower sides held at fixed temperatures, and there is no lateral heat flux. We use the notation $u_y = \mathrm{CSC}$ as a shorthand for

$$u_y = 0 \quad (y = 0, \Lambda), \qquad \frac{\partial u_y}{\partial x} = 0 \quad (x = 0, \lambda), \qquad \frac{\partial u_y}{\partial z} = 0 \qquad (z = 0,\ 1).$$

$$\text{(Cf. writing} \qquad u_y = \sum_{n=0}^{\infty}\sum_{m=1}^{\infty}\sum_{q=0}^{\infty} a_{nmq}\cos\frac{n\pi x}{\lambda}\sin\frac{m\pi y}{\Lambda}\cos q\pi z.)$$

The fields may then be written

$$\boldsymbol{u} = (\mathrm{SCC}, \mathrm{CSC}, \mathrm{CCS}), \quad \text{and} \quad T-(1-z) = \mathrm{CCS},$$

using obvious variants on the above.

A general linear stability analysis for this problem is given by Chandrasekhar (1961). Here we record that modes with a spatial structure given by

$$(n, m, q) = (1, 1, 1)$$

are unstable when

$$R > R^{(\mathrm{e})} = \frac{\pi^4\beta^6}{\beta^2-1}, \quad \beta^2 = 1 + \frac{1}{\lambda^2} + \frac{1}{\Lambda^2}.$$

Other possible flows include rolls with $(n,m,q) = (1,0,1)$ or $(0,1,1)$; setting $\Lambda^{-2}$ or $\lambda^{-2} = 0$ in the above gives the appropriate stability criteria. Varying the size of the box for the same modal structure shows that $R^{(\mathrm{e})}$ is least $R^{(\mathrm{e})} \approx 658$ when $\beta^2 = \frac{3}{2}$, implying that the rolls favour a wavelength $2^{\frac{1}{2}}$, and the (1, 1, 1)-flow prefers a longer wavelength, e.g. 2 for the square planform $\Lambda = \lambda = l$. Since we shall be primarily concerned with flows confined to a cube we remark that for $l = 1$, $R^{(\mathrm{e})} \approx 1315$, and for $\lambda^{-2} = 0$ and $\Lambda^2 = 1$, $R^{(\mathrm{e})} \approx 779$.

### 2.2. *Nonlinear analysis*

We seek a spatially truncated modal representation of the equations (2.1), guided like Lorenz (1963) by a solution to (2.1) which is a power series in $\epsilon = (R-R^{(\mathrm{e})})^{\frac{1}{2}}$ but where the first term is a (1, 1, 1)-mode. The fully three-dimensional problem is more difficult because a scalar representation of the velocity field is in general no longer possible. However solutions of the linearized version of (2.1) have $\omega_z = 0$, thus to keep the complexity of the ensuing algebra to an acceptable level, we choose $\boldsymbol{u}$ to be poloidal,

$$\boldsymbol{u} = \operatorname{curl}\operatorname{curl}[F_1(\boldsymbol{x})\,\hat{\boldsymbol{z}}].$$

Use of the vector identity

$$\hat{\boldsymbol{z}}\cdot\operatorname{curl}(\boldsymbol{u}_1\times\boldsymbol{\omega}_2) = \hat{\boldsymbol{z}}\cdot\operatorname{grad}(\nabla^2F_1)\times\operatorname{grad}(\nabla^2F_2),$$

where $\boldsymbol{u}_i = \operatorname{curl}\operatorname{curl}(F_i\,\hat{\boldsymbol{z}}),\quad i = 1, 2,\quad \boldsymbol{\omega}_i = \operatorname{curl}\boldsymbol{u}_i,$

shows there is no generation of vertical vorticity at second order (Schlüter *et al.* 1965; Jenkins & Proctor 1984). At third order a (1, 1, 1)-mode appears for which $\omega_z \neq 0$ unless we set $\lambda = \Lambda = l$, i.e. we have convection with square planform. All terms $O(\epsilon^4)$ are neglected.

Our model has $\boldsymbol{u} = \operatorname{curl}\operatorname{curl} F\hat{\boldsymbol{z}}$, where

$$\pi F = 4a(\tau)\cos\frac{\pi x}{l}\cos\frac{\pi y}{l}\sin\pi z + b(\tau)\left(\cos\frac{2\pi x}{l}+\cos\frac{2\pi y}{l}\right)\sin 2\pi z$$

and

$$\pi[T-(1-z)] = 4d(\tau)\cos\frac{\pi x}{l}\cos\frac{\pi y}{l}\sin\pi z + 2e(\tau)\sin 2\pi z + 4f(\tau)\left(\cos\frac{2\pi x}{l}+\cos\frac{2\pi y}{l}\right)\sin 2\pi z,$$

with $\tau = \pi^2 t l^{-2}$. In addition, we define $L = l^2+1$, $r = Rl^4/\{\pi^4(l^2+2)\}$, so that

$$\left.\begin{aligned} a' &= -\sigma(L+1)\,a+\sigma r d+2ab,\\ b' &= -4\sigma L b+\sigma r L^{-1}(L+1)f-L^{-1}(L+1)\,a^2,\\ d' &= -(L+1)\,d+a(2+4e+4f),\\ e' &= -4(L-1)\,e-4ad,\\ f' &= -4Lf+b-ad. \end{aligned}\right\} \tag{2.3}$$

Similar systems may presumably be derived for other symmetric planforms. Contrast (2.3) with the equation of Jenkins & Proctor (1984) for the identical problem with poorly conducting boundaries: their set is third-order because they choose (for reasons that are not entirely clear) a different ordering for the time derivative to that implied by (2.3). As they have chosen a planform rotated by 45° with respect to ours, they can, however, pronounce on the stability of that pattern to perturbations consisting of rolls.

Observe that we could recover the Lorenz equations by setting $b = f = 0$, except for the presence of the term in $a^2$ in the second equation. This represents vortex stretching, i.e. $(\boldsymbol{\omega}\cdot\operatorname{grad})\,\boldsymbol{u} \neq \boldsymbol{0}$, which excites mode $b$, and mode $f$ follows. This contrasts with the work of Toomre, Gough & Spiegel (1982), who choose a second mode *ad hoc*: their $\boldsymbol{u}$ for the square cell differs from ours. Further, they derive their model by considering only the $z$-component of the momentum equation: we expect a different one to arise from the $x$- or $y$-component.

If we now linearize about the steady solution $a = b = d = e = f = 0$, we see that the equations split into two pairs, one for $a$ and $d$ only, the other for $b$ and $f$. As might

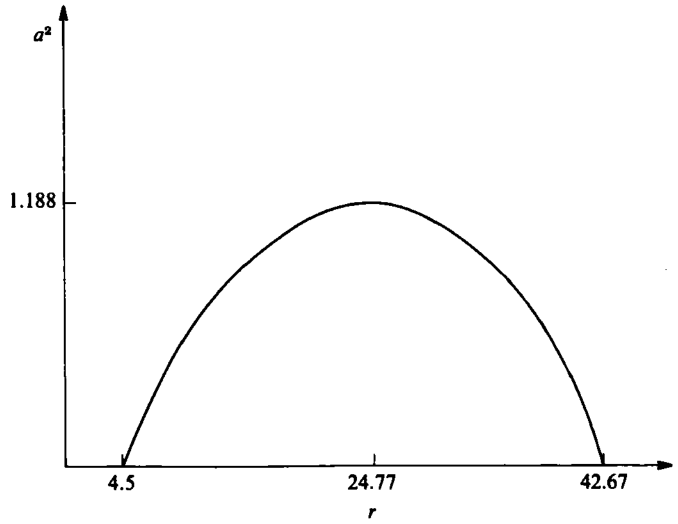

FIGURE 1. Sketch of steady-state amplitude $a^2$ as a function of Rayleigh number $r$ for the truncated system (2.3) with $l = \sigma = 1$.

be expected, the second pair gives the critical value $r = r^{(f)}$ which translates into $R$-critical for a (2, 0, 2) mode. There is therefore no advantage in copying Lorenz by defining $r$ so that $r = 1$ when $R = R^{(e)}$ – the normalization used, which is such that when $R = R^{(e)}$, $r = \frac{1}{2}(L+1)^2$, has been chosen to keep (2.3) as simple as possible.

Analysis which partly parallels that of Malkus & Veronis (1958) shows that (2.3) has a steady finite-amplitude solution of the form sketched in figure 1. For this $b$, $e$ and $f < 0$, but the signs of $a$ and $d$ are determined only by the condition that $ad > 0$. Numerical work, details of which may be published elsewhere, indicates this branch is stable throughout its length. Contours of $e(r, \sigma) =$ constant are drawn in figure 2 ($[-e]$ is a measure of the heat transport by the convection). Note the strong $\sigma$-dependence as $\sigma \to 0$, and that the heat transport decreases with $r$ for sufficiently large $r$. We expect the model to be misleading at these $r$.

### 2.3. *Spatial structure of the finite-amplitude flow*

We consider the velocity pattern given by $F$ above. If $a$ and $b$ are time-independent then streamlines of $\boldsymbol{u}$ are given by

$$\frac{\mathrm{d}\boldsymbol{x}}{\mathrm{d}p^*} = \boldsymbol{u}(\boldsymbol{x}(p^*)) = \operatorname{curl}\operatorname{curl}[F(\boldsymbol{x})\,\hat{\boldsymbol{z}}], \tag{2.4}$$

where $p^*$ is a parameter related to the turnover time. A non-dissipative set of equations such as this may usually be expressed in a Hamiltonian formalism as, for example, Whiteman (1977, pp. 1062–1063) explains: if we take as momentum variable

$$p_H = \int u_z \,\mathrm{d}y,$$

then $x$ is the conjugate coordinate and the role of time is played by $z$, i.e. the Hamiltonian $H$ then follows from the integration of $\mathrm{d}p_H/\mathrm{d}z = -\partial H/\partial x$. Arnold (1966, p. 347) appears to have been the first to suggest that three-dimensional fluid flows may therefore become ergodic in the same way that, for example, the Hénon–Heiles Hamiltonian is able to describe particle trajectories that fill finite volumes of phase

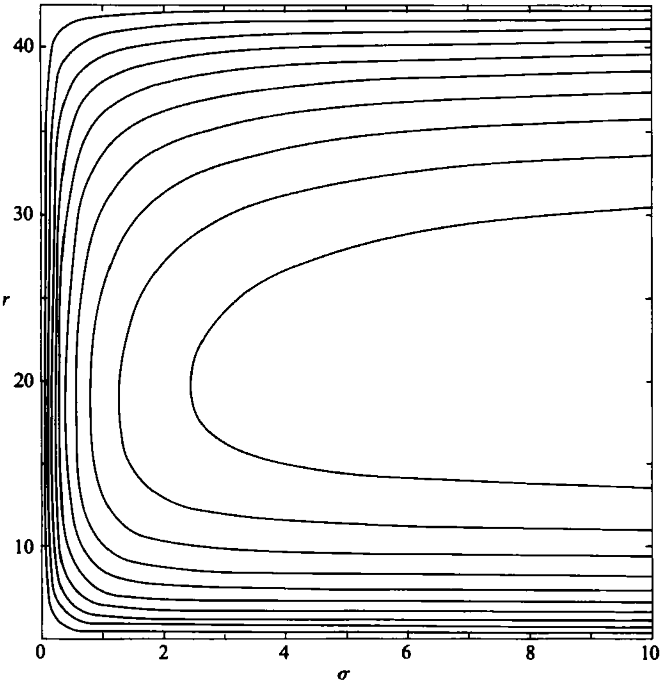

FIGURE 2. Steady $-e = \frac{1}{4}(N-1)$ as a function of $r$ and $\sigma$ for the truncated system (2.3). The contours are drawn at equally spaced values, with the maximum at centre right.

space (Whiteman 1977). Following Arnold, Hénon (1966) numerically calculated (semi)ergodic streamlines of a particular inviscid flow, the physical significance of which was not, however, demonstrated.

The usual analytic techniques of Hamiltonian theory do not apply straightforwardly (B. McNamara, private communication). Numerically, Arter (1983*b*) has verified that for the above system as $|b/a|$ increases from zero, regions where streamlines are ergodic do indeed develop and are prominent near surfaces which bound the convection. (When $a$ or $b$ is zero, streamlines are closed.)

The properties of the singular (stagnation) points $\boldsymbol{x}$ such that $\boldsymbol{u}(\boldsymbol{x}) = \boldsymbol{0}$ are of interest. To compare with Arter (1983*b*) we define $n = -b/a$ and confine our attention to the triangular prism $0 \leqslant x \leqslant \frac{1}{2}$, $x \leqslant y \leqslant 1-x$, $0 \leqslant z \leqslant 1$. $|\boldsymbol{u}| \neq 0$ inside the prism, except for $n = 0$, when the velocity vanishes on the lines $x = y = \frac{1}{2}$, $x = z = \frac{1}{2}$ and $y = z = \frac{1}{2}$. There are always singular points at its vertices and at the centre of the face $x = 0$; for $n > 0$, the stagnation point at $x = y = z = \frac{1}{2}$ is replaced by two nearby, on opposite faces of the prism. It may be easily shown that the flow on the face $y = 1-x$ is just that on $y = x$ after reflection in the plane $z = \frac{1}{2}$. We therefore study only the point $P_1$: $(x_1, y_1, z_1)$ given by

$$\begin{aligned}(c_1, c_2, c_3) &= \cos\pi(x_1+y_1,\ x_1-y_1,\ z_1)\\ &= \left(\frac{c_3}{2n},\ 1,\ \frac{1-(1+32n^2)^{\frac{1}{2}}}{8n}\right).\end{aligned}$$

(Taking the positive sign with the square root gives $|\cos\pi z_1| > 1$ unless $n > \frac{1}{2}$.) Near $P_1$, motion normal to $y = x$ is described by

$$\dot{Y} = -2Yc_3(1-c_3^2),$$

where $Y$ is a perturbation to $c_2$. Similarly, in the prism face we have that

$$\begin{pmatrix} \dot{X} \\ \dot{Z} \end{pmatrix} = \begin{pmatrix} 0 & (1-c_1^2)(1-8nc_3) \\ (1-c_3^2)(4nc_3-1) & (1-c_3^2)\,2c_3 \end{pmatrix} \begin{pmatrix} X \\ Z \end{pmatrix}.$$

Seeking solutions $\propto \exp(st)$, we find that $s > 0$ for the first equation and for the second, $s$ is complex with negative real part. Thus the flow in the prism face consists of a swirl into $P_1$. At any point near $P_1$, but not on $y = x$, there is a component of flow away from the face. (Motion near the stagnation point which appears when $n > \frac{1}{2}$ has an identical form under time-reversal.)

In the inviscid limit, it follows from the local theory of Arter (unpublished manuscript) that these structures are associated only with time-dependent motion. His model for inviscid flow near a stagnation point entails setting

$$T = Ux + Vy + Wz, \quad \boldsymbol{\omega} = (\psi, \chi, \phi),$$

where $U$, $V$, $W$, $\psi$, $\chi$ and $\phi$ depend only on $t$, and substituting into (2.1*b*) and (2.2) to give (after rescaling variables)

$$\dot{\chi} = V, \quad \dot{\psi} = -U, \quad \dot{\phi} = 0,$$
$$\dot{U} = -\phi V + \psi W, \quad \dot{V} = \phi U - \chi W, \quad \dot{W} = -\psi U + \chi V.$$

The only stable solutions of this system are oscillatory. However, at boundaries where some of the gradients of $\boldsymbol{u}$ and $T$ are fixed, this analysis does not apply. The stagnation point at, for example, the centre of the face $x = 0$ may therefore form a stable steady flow.

## 3. Computational techniques

### 3.1. *The numerical method*

The numerical analysis of the equations (2.1) breaks down into two parts. Obviously one is stepping the (hyperbolic) equations forward in time; the other is the solution of an elliptic Poisson equation for the pressure at each timestep to ensure $\operatorname{div} \boldsymbol{u} = 0$. Since three-dimensional calculations are expensive in terms of computer time, it is essential to pick the most efficient method and machine.

The ICL Distributed Array Processor (Hockney & Jesshope 1981) was chosen because much experience had been gained in its use (Arter 1983*a*, hereinafter referred to as paper A) and also it is particularly suitable for time-stepping large arrays. For a problem with periodic boundary conditions, the pseudospectral method (Orszag 1971) is usually to be preferred. However, this depends on the availability of high-speed Fourier-transform routines, usually written in assembly language. Such low-level routines are not provided on the DAP: its architecture is such that the speed-up relative to DAP-FORTRAN is insignificant. In these circumstances, finite-difference methods are competitive (Arter 1982), besides being easier to program. The scheme used is time- and space-centred with the DuFort–Frankel representation for diffusive terms, as first suggested by Roberts & Weiss (1966) (see also Peyret & Taylor 1983 §2.6.3).

Grötzbach (1982) has independently developed a very similar code. Like him, we also solve Poisson's equation for the pressure by transforming the fields to and from wavenumber space, where inverting the Laplacian is a trivial operation. The discussion of Peyret & Taylor (1983, §6.3.1) implies that because of our boundary condition $\boldsymbol{n} \cdot \operatorname{grad} p = 0$, where $\boldsymbol{n}$ is the surface normal, $p$ is expressible as a cosine series in each spatial variable. We can use the algorithms of Cooley, Lewis & Welch (1970) to reduce the arithmetic required.

However, the use of a leapfrog scheme means that only alternate grid-points are defined at each timestep. Thus before Fourier-transforming we have to interpolate for the other half of the mesh, using a fourth-order formula (Moore, Peckover & Weiss 1973). In addition, we use a $24 \times 24 \times 24$ grid, yet the DAP is physically a $64 \times 64$ processor array. The fields have to be carefully arranged in store, and dislocated in one coordinate direction (S. F. Reddaway, private communication) to make the best use of the computer.

There is a subtle point concerning the numerically obtained solutions. We must realize that as far as the code is concerned a statement such as $T-(1-z) = \mathrm{CCS}$ does not constrain the higher derivatives of $T$. Similarly, although all odd derivatives of $p$ necessarily vanish at the boundaries, since the scheme is second-order this $p$ is consistent with all $\rho$- and $\boldsymbol{u}$-fields that do not drive $\boldsymbol{n}\cdot\operatorname{grad} p \neq 0$ by, for example, their nonlinear interactions. In particular, it is possible to take $\rho \propto T^2$, $T-(1-z) = \mathrm{CCS}$, despite the apparent conflict with the modal expansion for $\boldsymbol{u}$ given in §2.1.

### 3.2. *Validation of the program*

This large code has been thoroughly validated as described by Arter (1982). As in paper A, the two-dimensional codes of Moore *et al.* (1973) have been successfully used to test the complete program when initial variation with one or other horizontal coordinate is suppressed. The code thereby demonstrates a dependence on the starting conditions, since the rolls obtained appear to be stable at parameters where motions with square planform are found. Further, a numerical solution decays when started with a fully three-dimensional velocity pattern at $R = 1000$, although rolls exist for $R > 779$. Grötzbach (1982) also notes similar difficulties, which need not be entirely numerical (see e.g. Busse 1978). Otherwise, the results again suggest the primitive variable formulation is slightly superior to that used by Moore *et al.* (1973): we find that point values of the computed solutions differ most where there are large gradients of $\psi_{\mathrm{p}}$, the two-dimensional flow potential. The discrepancies are such that better agreement with our $\boldsymbol{u}$ is obtained by using higher-order difference representations of curl $(0, \psi_{\mathrm{p}}, 0)$. Since the $T$-fields are practically identical, we derive values for the total heat transport $N$ closer to those found using the finer two-dimensional meshes.

Lastly we discuss the question of when the numerical results cease to be good representations of the solutions of (2.1). Unfortunately, owing to the complexity of the code needed to perform the Fourier transforms, it has not been possible to consider mesh sizes other than $24^3$. Computations on significantly larger meshes are beyond the DAP's present capabilities (the current ones take 30–90 min of DAP time) and it is not clear that studying grids coarser than $24^3$ would be of value commensurate with the programming effort involved. Grötzbach (1983) has recently verified that the criterion for two dimensions derived by MW applies, namely that a numerical solution is *qualitatively* correct provided every boundary layer is at least three mesh-intervals wide.

Further experience with the code of paper A (Arter 1984*a*) argues that this is pessimistic, and the 'three-points' test should be applied only to the significant field components in the dominant features of a flow. It is not easy to program the test because of the subjective element this introduces, so we write a code that examines the variation of each field component for any two coordinates held constant, e.g. $f(z) = u_y(x, y, z)$. It then discovers the two points in $z$ between which occurs the largest

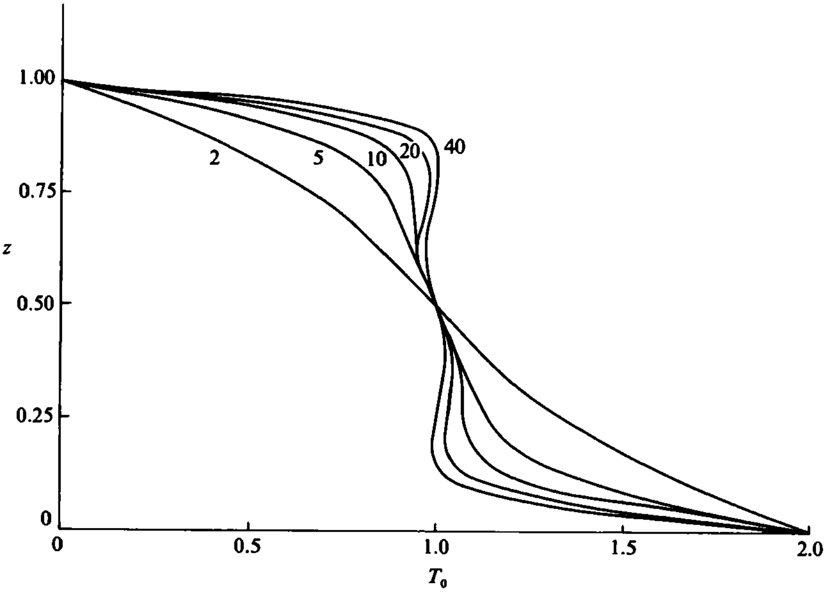

FIGURE 3. Plots of horizontally averaged temperature $T_0(z)$ for $\sigma = 1$; varying $R$ marked on the curves in units of thousands.

monotonic change in $f$, and flags if more than half of this is confined to one mesh interval. Of the $\boldsymbol{u}(\boldsymbol{x})$ presented in this paper only the accuracy of that for $\sigma = 0.05$ and $l = 2\frac{1}{8}$ is thereby declared suspect: $T(z)$ is flagged for $z$ close to boundaries for $R \geqslant 10000$ and $\sigma = 1$, but we believe that the 'three-points' criterion is not violated there until $R$ approaches 60000.

## 4. Numerical experiments at unit Prandtl number

### 4.1. *Phenomenology*

The series of calculations for $\sigma = 1$ was begun at $R = 25000$ using an $O(1)$-amplitude velocity pattern with the (1, 1, 1) modal structure predicted by linear theory. No perturbation was made to the temperature distribution. The resulting steady three-dimensional solution (which was reached on a turnover timescale) was used to start computations at $R = 20000$ and 30000 and so on for $R$ down to 15000 and up to 60000, for which the flow has structure as fine as the mesh spacing. A second set of calculations covered $R = 3500$–10000, beginning with $R = 5000$, and solutions for $R = 1500$ and 2000 were computed separately.

Almost all properties of the results showed a monotone variation as $R$ was increased. In figure 3 the graphs of $T_0(z)$, horizontally averaged temperature $T$, indicate the development of isothermal regions away from the horizontal boundaries. They share this feature with the results for rolls (Veronis 1966), although $T_0(z)$ for the three-dimensional solutions remains monotone over a greater range of $R$. Further, the second change in sign of $\mathrm{d}T_0/\mathrm{d}z$ in $z > \frac{1}{2}$ for $R > 10000$ is not seen in the two-dimensional results even at much larger $R$ (MW) or in the axisymmetric case (JMW). Figure 4 reveals more: it shows a plot of vertically averaged temperature $\overline{T}(x, y)$ within the square $0 \leqslant x, y \leqslant 2$, for $R = 30000$. The regions enclosed by the extremal contours have become X-shaped to give a pattern which, when rotated

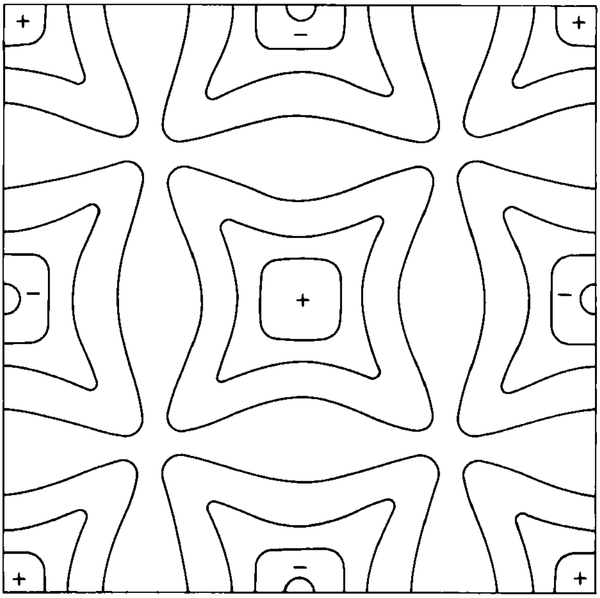

FIGURE 4. Vertically averaged temperature for $\sigma = 1$, $R = 30000$. The contours are drawn at equally spaced intervals; regions marked + contain the highest values, those marked − the lowest. The area covered is $0 \leqslant x, y \leqslant 2$, i.e. 4 times that used in figure 5.

through 45°, resembles figure 11 of Busse (1978). That 'shadowgraph' was obtained experimentally, and, although tricky optical effects are at work, it is essentially a measure of $\overline{T}(x, y)$. Thus, despite their different boundary conditions, the flows described in this section appear to have laboratory counterparts.

Unlike experimenters, we may produce three-dimensional plots of isothermal surfaces (figure 5). These help us to understand why $\mathrm{d}T_0/\mathrm{d}z$ changes sign and also serve to illustrate important properties of the flow field $\boldsymbol{u}$. We see that the pattern of convection is generated by a volume with base area 2, and has eightfold symmetry (cf. Veronis 1966). Note that we could equally consider a volume (e.g. $-1 \leqslant x \pm y \leqslant 1$) centred on a region where isotherms are displaced upwards, implying rising flow, or one with $u_z < 0$ at the middle. The flow is topologically two-dimensional (Stuart 1964; Drobyshevski & Yuferev 1974).

Nevertheless $\boldsymbol{u}(x, y, z)$ has three components, so it is difficult to understand its detailed properties. The graphics used in paper A are not very helpful because the surfaces $\boldsymbol{u}^2 =$ constant distort very little as $R$ varies. We note though that the maxima of $\boldsymbol{u}^2$ on the vertical edges are displaced with respect to $z = \frac{1}{2}$: however, the asymmetry diminishes as $R$ increases. Plotting streamlines on the vertical planes of symmetry is more revealing (figure 6).

Flow neither enters nor leaves them, but since $\partial u_z/\partial z \neq 0$ there, the lines need not be closed. On the planes $y = x$ and $y = 1-x$ they reveal the usefulness of the truncated modal expansion. We expect that greater $R$ should lead to increased importance of the second-order mode, represented by $n$ (§ 2.3), and thus that the spiral attractors shown in figure 6 should tighten and move from the midplane $z = \frac{1}{2}$ as $R$ increases. Indeed, they do so as $R$ changes from 1500 to 2000, and this trend continues up to the highest $R$ studied. Note that, even for $R$ as small as 1500, $Re = O(10)$ and the model cannot be formally justified. Nonetheless it also successfully predicts the

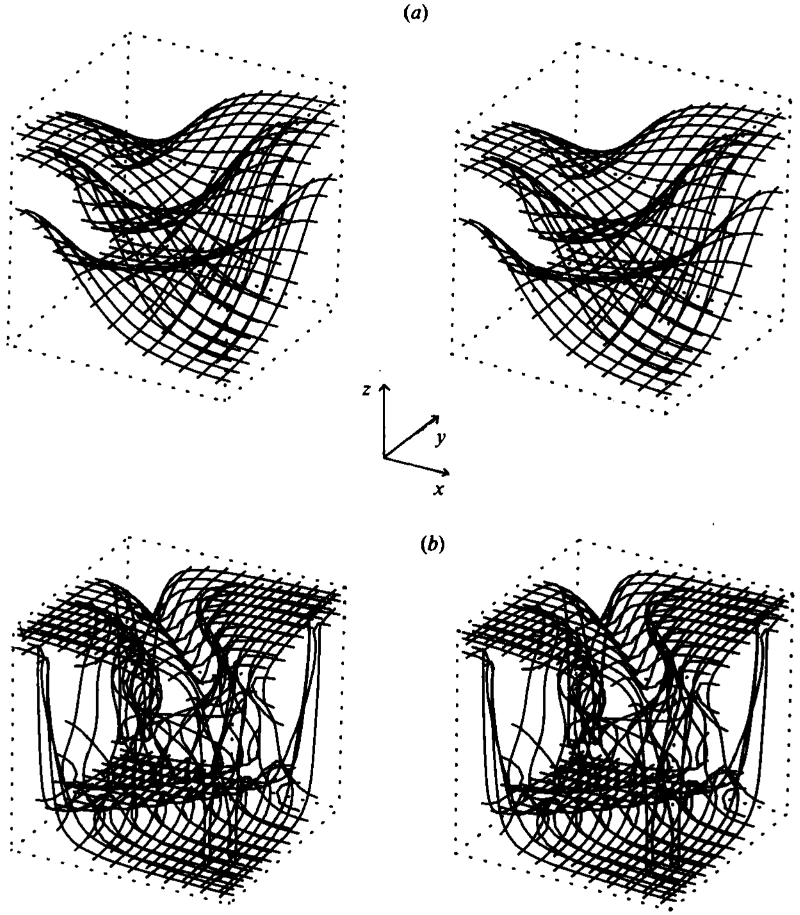

FIGURE 5. Stereo plots showing surfaces of constant temperature $T = \frac{1}{4}, \frac{1}{2}$ and $\frac{3}{4}$ for steady solutions with $\sigma = 1$ and (a) $R = 2000$, (b) $R = 20000$. The maximum value surface is the lowest, the minimum the highest on the left- and right-hand edges of the (unit) cube. To view, hold a stereo pair at 15–30 cm distance, one image before each eye, with eyes relaxed to focus at infinity. Three, not four images should be seen, and the central one, which may at first appear out of focus, gives an accurate impression of depth.

appearance and spread of regions where streamlines are seemingly ergodic (see figure 7). Some structure can, however, be made out even at $R = 30000$. For a particular field-line, the average value of the turnover time $t_1$, defined as the interval between successive transits by a test particle of the plane $z = \frac{1}{2}$, suffices to determine whether it is ergodic. For such paths $t_1 \approx 2.5$–$2.7$ on average (using units where the maximum of $u_z$, $u_{zm} = 1$), otherwise the average $t_1 \approx 1.9$–$2.1$. In Arter (1983*b*), unlike here, these two $t_1$ diverged as the equivalent of $R$ increased.

The change in the vorticity-squared distribution $\omega^2$ is more marked than for $\boldsymbol{u}^2$ (MW, JMW), although sadly the three-dimensional contours are not easily followed, even using colour graphics and stereopsis. Nevertheless they confirm the impression one may derive from figure 6, namely that, at low $R$, $\omega^2$ is maximum on the vertical faces of the unit cube drawn in figure 5, but as $R$ is raised the distribution changes so that the maxima lie in the spiral attractors and peak sharply there. At all $R$, large $\omega^2$ is associated with regions of reduced $\boldsymbol{u}^2$.

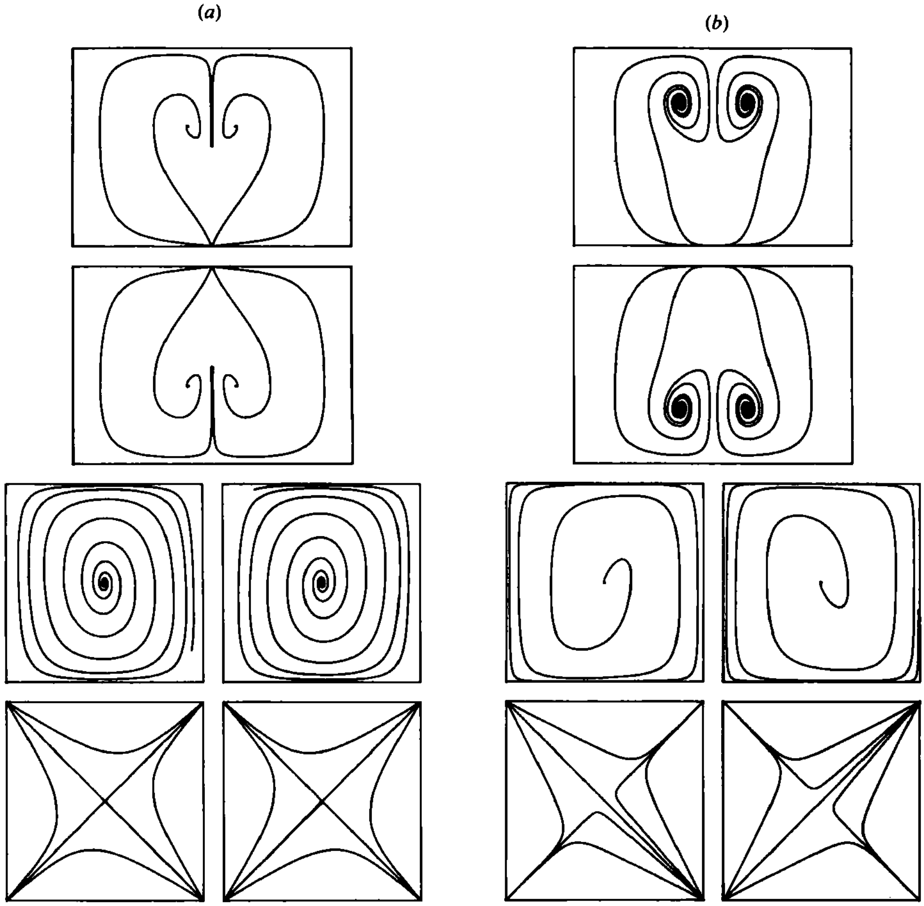

FIGURE 6. Streamlines of steady flow for $\sigma = 1$ and (a) $R = 2000$, (b) $R = 20000$, drawn for $0 \leqslant x, y, z \leqslant 1$ in the planes $z = 0$ (bottom left), $z = 1$ (bottom right); $y = 0, 1$; $y = 1-x$ and $y = x$ (top).

Although the initial velocity perturbation possesses no vertical vorticity, the numerical solutions have $\omega_{zm} \neq 0$ (m denotes maximum absolute value). A relative measure $r_\omega = \omega_{zm}/u_{zm}$ grows rapidly with $R$, from 0.0024 to 0.35 as $R$ increases from 3500 to 15000. Figure 8 shows a typical distribution of $\omega_z^2$ for moderate $Re = 26.8$. It is clear that modes (e.g. (2, 2, 3)) with a different spatial structure to those of the truncated system will be needed to represent this – such an extended model will probably be too complicated to be of much use. At large $R$, $\omega_z^2$ develops even more contorted structure, although its gradients are not as large as those of $\boldsymbol{\omega}^2$, and the two have their maxima in disjoint regions, reflecting that $\omega_z^2$ is significantly smaller than $\omega_x^2+\omega_y^2$.

Let us look at the steady vorticity equation in detail. Taking the curl of the momentum equation and non-dimensionalizing with respect to the turnover time yields

$$0 = \mathrm{Re}\,\mathrm{curl}\,(\boldsymbol{u}\times\boldsymbol{\omega}) + \frac{R}{\sigma}\hat{\boldsymbol{z}}\times\mathrm{grad}\,T - \nabla^2\boldsymbol{\omega}.$$

We see that in isothermal regions where the diffusion of $\boldsymbol{\omega}$ might be expected to be small, such as the middle of cube faces, $\boldsymbol{u}\times\boldsymbol{\omega} = \mathrm{grad}\,\Phi$ for some $\Phi$. Since $\boldsymbol{u}$ is ergodic,

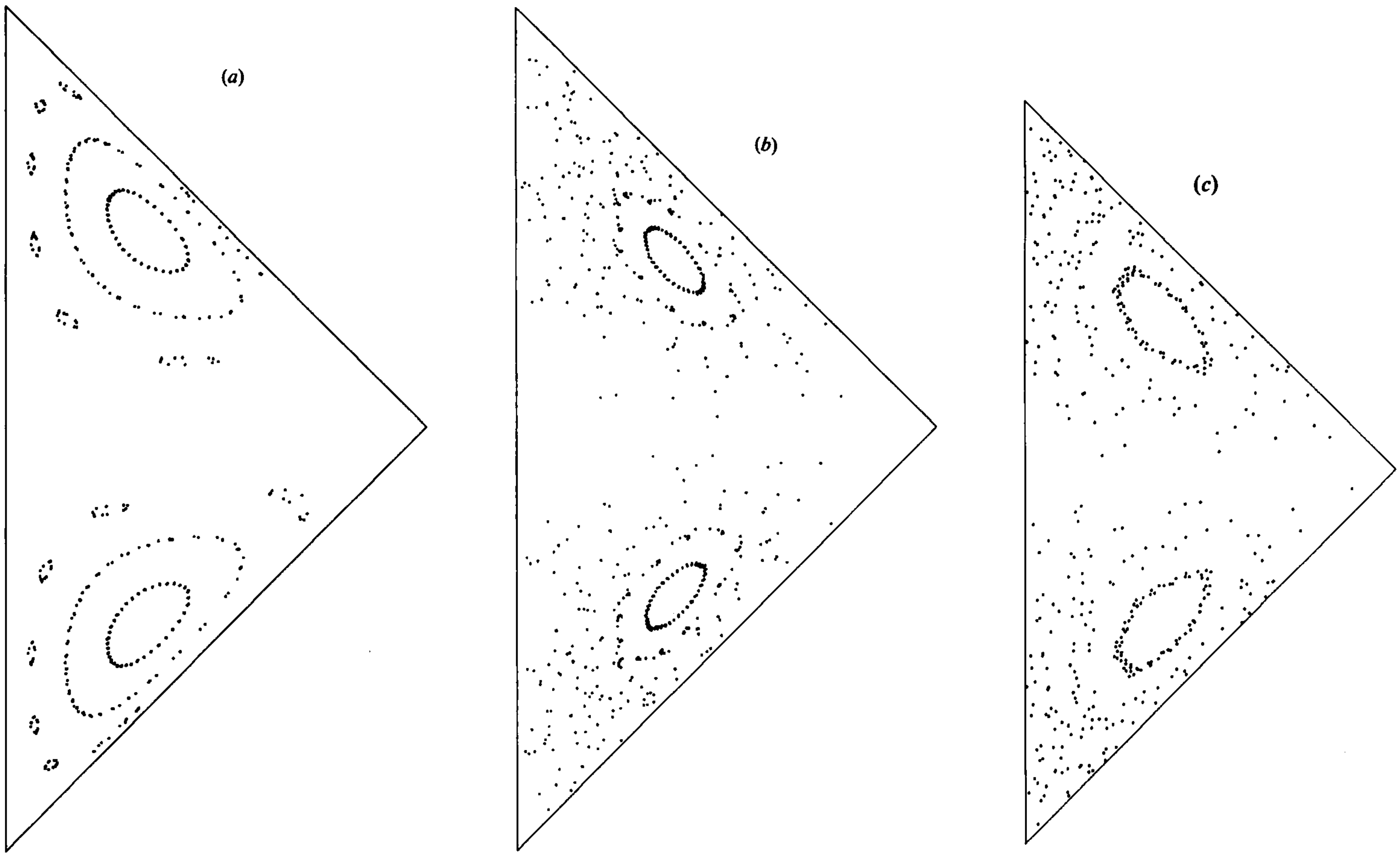

FIGURE 7. Plots of 150 intersections of 4 streamlines with the midplane $z = \frac{1}{2}$ for flows $\sigma = 1$ and (*a*) $R = 2000$, (*b*) $R = 10000$, (*c*) $\sigma = 0.1$ and $R = 2000$. The region shown is the quarter-cell $x \leqslant y \leqslant 1-x$, $0 \leqslant x \leqslant \frac{1}{2}$. Flow ascends in the bottom half of the diagram and falls in the top.

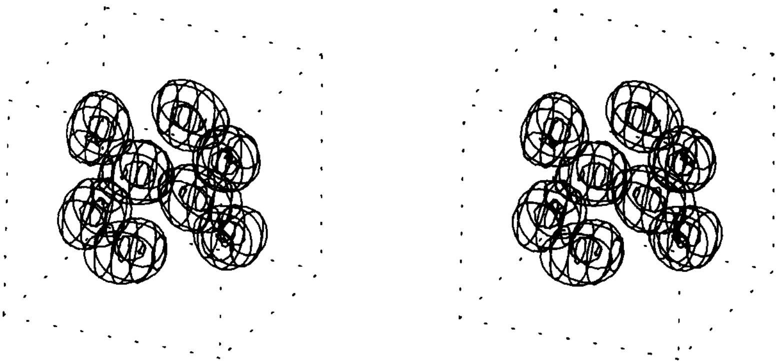

FIGURE 8. Stereo plot of surfaces $\omega_z^2 = 0.25$ and 0.8 in units of $\omega_{zm}^2$, for $R = 3500$ and $\sigma = 1$. The surfaces of higher $\omega_z^2$ all lie within those of the smaller value.

however, $\Phi = 0$ (Arnold 1972), and as the imposed boundary conditions prevent $\boldsymbol{\omega} \parallel \boldsymbol{u}$, $\boldsymbol{\omega}$ must be small as $Re \rightarrow \infty$, in agreement with numerical calculation. Figure 9 reveals the spatial distributions of the vector amplitudes $V_1$, $V_2$ and $V_3$ of the above three terms in the vorticity equation at $R = 10000$. All have maxima in the region of the spiral attractors. At lower and higher $R$, the secondary features of $V_1$ become more prominent, and $V_3$ also becomes relatively greater in those regions. Vorticity generation ($V_2$) takes place outside the volumes where $V_3$ is largest; thus there is need for transport ($V_1$). It is remarkable that, unlike MW and JMW, the vertical plumes are not the dominant source of $V_2$, as cursory inspection of the isotherms in figure 5 would suggest. This effect which is associated with the formation of layers where $T$ varies as $\exp(-z)$ (§4.2), distinguishes the square from two-dimensional and circular planforms.

On a last descriptive note, we show in figure 10 plots of the four terms defined by Lipps (1976), after Deardorff & Willis (1967), appearing in the horizontally averaged kinetic-energy equation. In our notation these terms are

$$T_1 = \sigma R \langle u_z[T-(1-z)]\rangle, \quad T_2 = -\frac{\partial}{\partial z}\langle u_z(p+\tfrac{1}{2}\boldsymbol{u}^2)\rangle,$$

$$T_3 = \sigma \frac{\partial^2}{\partial z^2}\langle \tfrac{1}{2}\boldsymbol{u}^2\rangle, \qquad T_4 = -\sigma\left\langle \frac{\partial u_i}{\partial x_j}\frac{\partial u_i}{\partial x_j}\right\rangle.$$

We see that essentially the production term $T_1$ balances the dissipation $T_4$, except near the boundaries where $T_2 + T_4 \approx 0$, and that $|T_3|$ is everywhere small. The only contrast with Lipps' results (despite their time-dependence) is that we find $T_2 > 0$ (and $T_3 < 0$) at the edges $z = 0, 1$, apparently because our flow lacks a viscous boundary layer – this $T_i$ behaviour is predicted by the truncated model. Lipps (1976) considers other statistics of his numerical experiments, which are for $\sigma = 0.7$. We suggest that our graphics, since they provide local information about the relative importance of the various terms in the governing equations, give a better insight into the physics of the solutions. Further, here the planform is fixed by our choice of initial conditions (see §6).

### 4.2. *Asymptotics and Nusselt-number variation*

The thermal layers which develop at high $R$ may be tested for simple functional dependences provided they form near the boundaries of the computational box or 'cube'. The number of meshpoints used is only 24 in each direction; therefore the results derived cannot be very accurate.

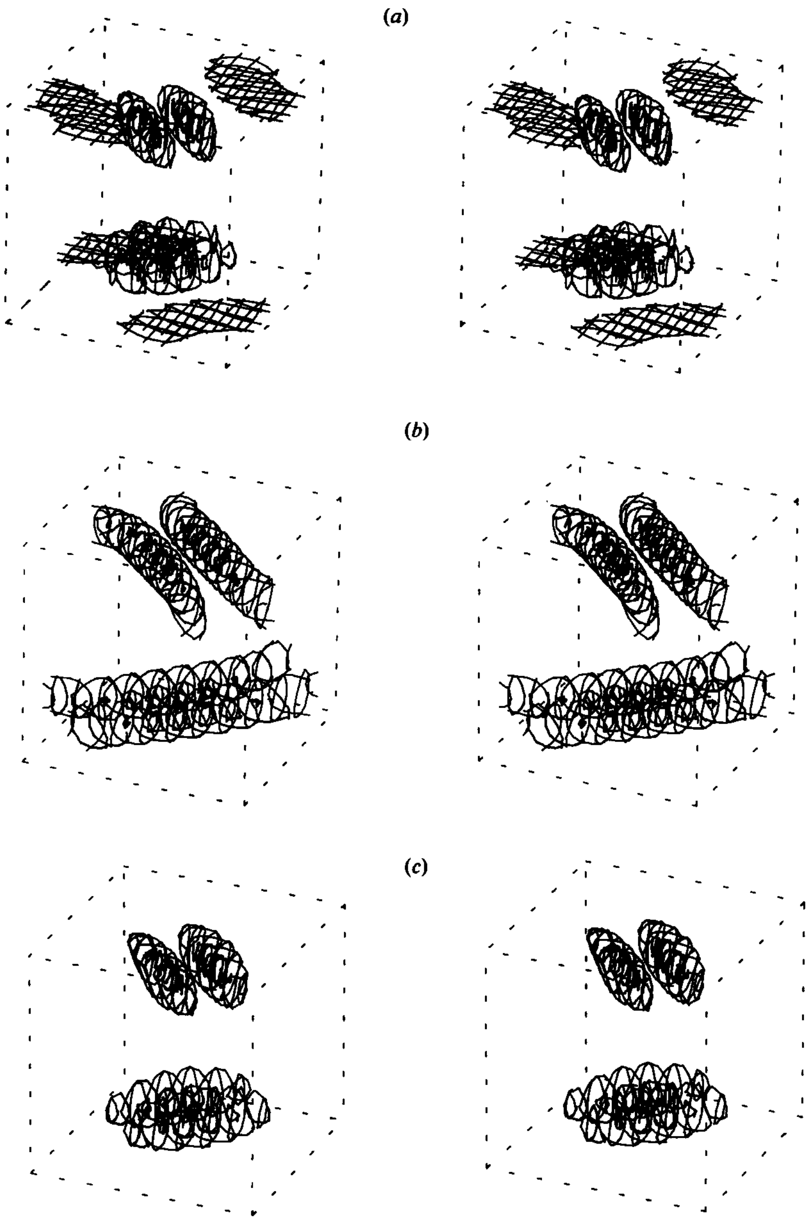

FIGURE 9. Stereo plots of the magnitudes of the terms in the vorticity balance equation. The surfaces are drawn for values 70% and 90% of maximum. (*a*), (*b*) and (*c*) show $V_1 = Re\,|\,\mathrm{curl}\,(\boldsymbol{u}\times\boldsymbol{\omega})\,|$, $V_2 = R\sigma^{-1}\,|\,\hat{\boldsymbol{z}}\times\mathrm{grad}\,T\,|$ and $V_3 = |\nabla^2\boldsymbol{\omega}|$ respectively. The higher-value surfaces are each contained by one of lower value. $R = 10000$ and $\sigma = 1$.

We find that the layers near the vertical edges of the cube have the expected Gaussian form at high Péclet number $Pe = \sigma\,Re$, which may be summarized as

$$T(x, 0, \tfrac{1}{2}) \sim \exp\,(-\tfrac{1}{8}Pe\,x^2).$$

However, the structure of $T$ near the upper and lower edges of the face $x = 0$ is not so easily described, although a measure of layer thickness has the same scaling: the distance $\delta_*$ along the line $y = \frac{1}{2}$ between the edge and the point where $T$ is halved

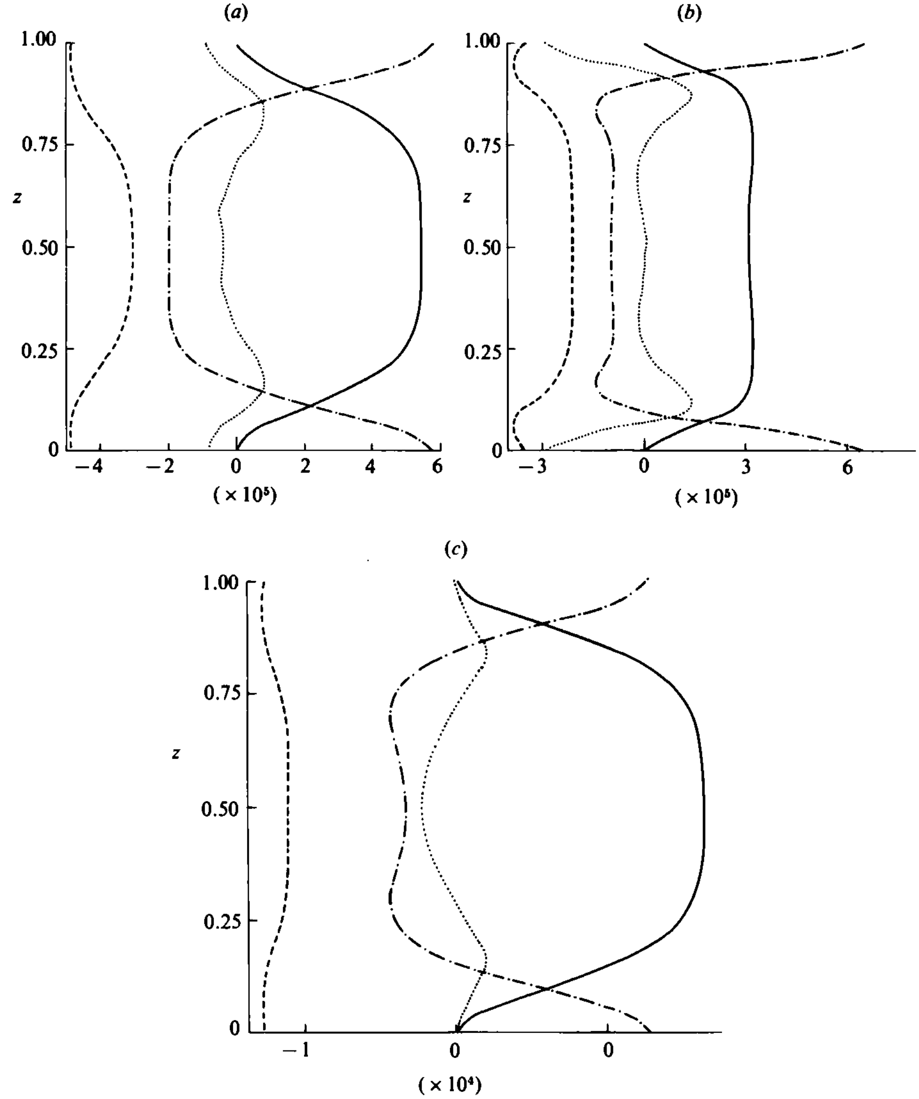

FIGURE 10. The vertical variation of $T_1$ (solid line), $T_2$ (dash–dot), $T_3$ (dotted) and $T_4$ (dashed) for (*a*) $\sigma = 1$, $R = 3500$, (*b*) $\sigma = 1$, $R = 40000$ and (*c*) $\sigma = 5$, $R = 5000$. $T_1$ represents the production, $T_2$ the diffusion, $T_3$ the molecular transfer and $T_4$ the dissipation of horizontally averaged kinetic energy (after Lipps 1976).

satisfies $\delta_* \sim 0.9 \times Pe^{-\frac{1}{2}}$. It follows that the plumes are more than twice as broad as their horizontal counterparts: MW find a factor of 1.7.

It is surprising that along the bottom diagonal of the cube, $T$ decays exponentially with $z$ away from $z = 0$, so that

$$T(x, x, z) \approx \exp\left[-z/\delta_1(x, R)\right],$$

where $\delta_1$ depends only weakly upon $R$, and $\delta_1(0) \approx 2$, $\delta_1(\frac{1}{4}) \approx 0.6$. The exponential dependence suggests that, since $u_z(x, y, 0) = 0$, the diffusive term is locally unimportant so $\boldsymbol{u} \cdot \mathrm{grad}\, T \approx 0$ and the flow is along isotherms. Figures 5 and 6 confirm this.

Of considerable importance is the variation of the Nusselt number $N$, a dimensionless measure of the heat transport, as a function of $R$. Values of $N$, $Pe$ and $Re$ for all the runs made are listed in the Appendix, and $N(R)$ is plotted for $\sigma = 1$ in figure 13(*a*), together with similar results for rolls of unit wavelength. We see that for low $R$, besides the three-dimensional motions having a greater critical $R$, their $\mathrm{d}N/\mathrm{d}R$ is also smaller, as predicted analytically (Malkus & Veronis 1958). In the nonlinear regime, $\mathrm{d}N/\mathrm{d}R$ for rolls declines more rapidly, however, so that the heat transports are equal to within the accuracy of the calculation for $R \geqslant 10000$.

At large $R$, $N(R)$ does not seem to be a simple power law: $\mathrm{d}\ln N/\mathrm{d}\ln R$ declines with $R$ up to $R = 60000$. This may be because the mesh size is not sufficiently great, so that $N$ is systematically reduced at large $R$, as in MW; or because $N$ has an additional logarithmic dependence. Since measures of the flow structure, e.g. $u_{z\mathrm{m}}/u_{x\mathrm{m}}$ and $u_{y\mathrm{m}}/u_{x\mathrm{m}}$ are practically constant ($\approx 1.27$ and $1.0$ respectively for $R \geqslant 10000$), the latter seems more likely. If, however, this effect is neglected, $N \propto R^{0.3}$ is a crude fit to the numerical results – and $Re = Pe \propto R^{0.6}$ to the same accuracy.

The only analytical study of three-dimensional convection at large $R$ for $\sigma = O(1)$ appears to be that of Riahi (1981). Comparison is difficult, because Riahi studies motions with a single wavelength, and the coupling constant $C$ that appears in his formulae is zero for square cells. He does however predict that $N \propto R^{\frac{3}{10}} (\ln R)^{\frac{1}{10}}$ for moderate values of $\sigma$, which is not inconsistent with our results.

## 5. Prandtl-number variation

When $\sigma$, the ratio of thermal to viscous diffusion, is not equal to unity, a number of purely computational constraints have to be considered. Even for the calculations described in this section where steady solutions are generally reached in a few turnover times, the *machine* time required to reach equilibrium scales roughly as $\max(\sigma, \sigma^{-1})$ because the numerical scheme is explicit. It is consequently uneconomic to study very large or small Prandtl numbers, although we can and have reduced costs in some cases by extrapolating to steady-state $N$, $Re$- and $Pe$-values from slowly converging data. In addition, we should especially like to obtain solutions for $Re$, $Pe \gg 1$ and $\sigma \ll 1$, because this is the astrophysically relevant regime (see e.g. Gough 1977). Although $Pe \gtrsim O(30)$ is adequate for many purposes (cf. Weiss 1966), $Re = \sigma^{-1} Pe \gtrsim 300$ if e.g. $\sigma = 0.1$. From the results for $\sigma = 1$ we should expect a mesh with only 24 points in each direction to become unable to represent $T$- or $\boldsymbol{u}$-fields when respectively $Pe$ or $Re$ reaches just such values. Our results for $\sigma < 1$ must therefore be regarded as tentative. We have not attempted to study the corresponding regime with $\sigma \gg 1$.

### 5.1. $\sigma > 1$

Three runs were made at $R = 5000$ for $\sigma = 2$, 5 and 10, each starting with the perturbation velocity pattern described in §4.1. The steady $T$-fields obtained were all very similar, and resembled that found when $\sigma = 1$, reflecting that the value of $Pe$ is practically independent of $\sigma$ at constant $R$. This also indicates there can be no great variation in the form of $\boldsymbol{u}$. Nevertheless, in agreement with the predictions of the truncated model, the spirally attracting stagnation points of the velocity field move closer to the midplane $z = \frac{1}{2}$ as $\sigma$ increases. They also weaken, and for $\sigma \geqslant 5$ the vorticity maxima lie on the vertical faces of the unit cube.

We should expect the structure of $\boldsymbol{u}$ to become simpler because of the decrease in Reynolds number $Re = \sigma^{-1} Pe$. Indeed, the Poincaré-type plots of $\boldsymbol{u}$ reveal that the ergodic regions have shrunk and are to be found only near the quarter-cell boundaries. Further, $T_3$, which measures second gradients of $\boldsymbol{u}^2$, becomes negligible, and for $\sigma > 2$ no longer changes sign near $z = 0$ and 1 (figure 10*c*).

The vertical vorticity measured by $r_\omega = \omega_{zm}/u_{zm}$ is also small: $r_\omega \approx 10^{-5}$ when $\sigma = 5$. Coupled with this is a reduction in the relative importance of the transport term $V_1$ in the vorticity equation. The analogue of figure 9 shows that the dominant balance is between generation $V_2$ and dissipation $V_3$, and this takes place in the regions of spirally attracting flow. We conclude that we have entered the viscous regime (MW, JMW) associated with $Re < O(1)$. Note that $N$ is almost independent of $\sigma$, just as in those two papers and also experimentally. Despite the comparatively minor role played by the thermal plumes here, it seems that the chief physical processes operate much as described by MW. Taking into account the restrictions upon our geometry and the cautionary remarks made at the start of this section, it does not seem desirable to explore this region of parameter space any further.

### 5.2. $\sigma < 1$ *and* $R = 5000$

In contrast with the small gradients of $\boldsymbol{u}$ seen at high Prandtl number, the small-$\sigma$ results are notable for their finely structured velocity fields. Nonetheless the temperature field shows little variation as $\sigma$ declines: $T(x, x, z)$ still shows exponential decay near $z = 0$. The lengthscale $\delta_2(x, \sigma)$ of the decay is only a weak function of $\sigma$; indeed $\delta_2(0, \sigma)$ scarcely changes in the range of $\sigma$ studied. It does, however, become harder to identify Gaussian profiles in the other thermal boundary layers, as a result of their broadening: when $\sigma = 0.05$ the effective Péclet number falls to $O(10)$. Only towards one end (e.g. $(0, 0, \frac{3}{4})$) of the thermal plumes is a (horizontal) Gaussian dependence clear for $\sigma \leqslant 0.1$, and the plume thickness grows like $Pe^{-\frac{1}{2}}$ as in §4.2.

Plotting $\boldsymbol{u}^2$ reveals changes, particularly in the minimum kinetic energy $K$-contour. When $\sigma = O(1)$, besides small regions near the corners of the unit cube, this encloses the lines $x = y = \frac{1}{2}$, $x = z = \frac{1}{2}$ and $y = z = \frac{1}{2}$. Motion grows in the vicinity of the centre $x = y = z = \frac{1}{2}$ as $\sigma$ gets smaller, and the surface contorts and changes its topology, although it remains connected. In planes $z \approx \frac{1}{4}$ flow is small near the lines joining the vertical faces $x = 0$ with $y = 1$ and $y = 0$ with $x = 1$, but, in $z \approx \frac{3}{4}$, $K$ is least along lines perpendicular to these. The intersection of the minimum $K$-contour with each vertical face has a curious inclined dumbell-like form.

Similar features are seen at high $R$ for $\sigma = 1$, but the small-$\sigma$ results take us up to greater effective $Re$. The size of $Re$ determines how pronounced is the spatial variation of the smallest $K$-contour, and $\sigma = 0.2$, $R = 5000$ has the same $Re$ as $R = 30000$, $\sigma = 1$, for example. These two solutions resemble each other very closely in other ways: their steady $\boldsymbol{u}$ are almost ergodic, the averages $T_i$, $i = 1, \ldots, 4$ (§4.1) have the same relative values, and their vorticity distributions are similar. This correspondence is explained by study of the vorticity-balance equation, which shows that $V_2$, the only thermal term, is smaller than $V_1$ and $V_3$. The final state is still reached on the turnover timescale at small $\sigma$, although $N(t)$ now monotonically approaches its steady value, unlike when $\sigma > 1$.

The dependence of steady $N$ and $Re$ upon $\sigma$ as $\sigma \to 0$ has been the subject of much study. The model of §2.2 predicts that for $\sigma \ll 1$ and $r = O(1)$, $a \propto \sigma$, i.e. $Re = O(1)$. $N = 1 - 4e$, where $(-e)\,a^{-2} = O(1)$; hence, when $\sigma \ll 1$, $N - 1 \propto \sigma^2$ (a result essentially due to Malkus & Veronis 1958). Our numerical results for $\sigma \geqslant 0.05$ are approximately fitted by $Re \sim \sigma^{-\frac{1}{2}}$, suggesting that the simple model is invalid. This is scarcely surprising since the convoluted structure of the computed $\boldsymbol{u}$ and $\boldsymbol{\omega}$ is so different from that predicted by it. Indeed, if we attempt by reducing $\sigma$ still further to understand

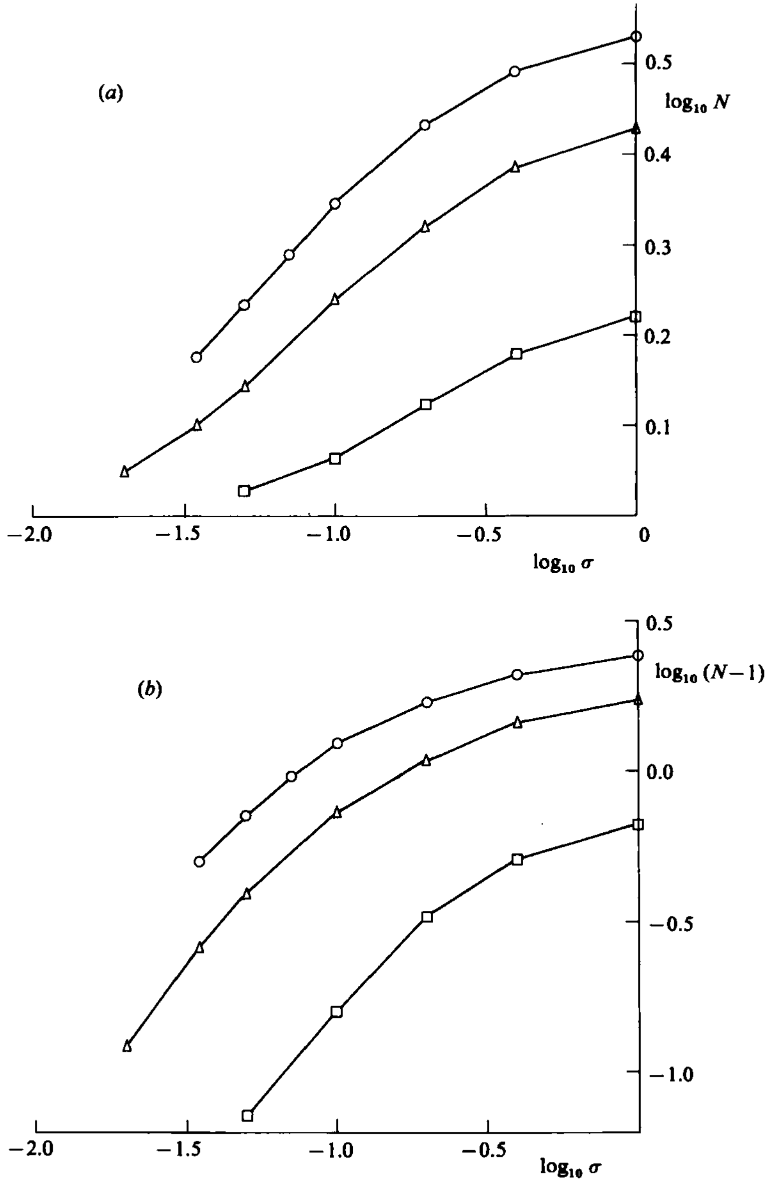

FIGURE 11. (*a*) Plot of $\log_{10} N$ as a function of $\log_{10} \sigma$ for $R = 2000$ (marked as squares), 3500 (triangles) and 5000 (circles). (*b*) is as (*a*) but drawn for $\log_{10}(N-1)$ versus $\log_{10} \sigma$.

why $Re$ at $\sigma = 0.035$ is discrepant, we find our numerical scheme breaks down (very sharp gradients of $\omega^2$ are associated with $Re \gtrsim 300$). This is frustrating, because $N$ also seems to change its functional dependence on $\sigma$ near this point.

Physically, $Re \approx \sigma^{-\frac{1}{2}}$ corresponds to convection at the reduced free-fall velocity. This we can show by returning briefly to dimensional notation. We have $u_0 d/\nu \approx (\kappa/\nu)^{\frac{1}{2}}$, i.e. $u_0^2 d^2 \sim \kappa\nu$, and $R$ = constant is equivalent to $g\alpha \Delta T d^3 \sim \kappa\nu$; hence $u_0^2 \sim g\alpha \Delta T d$. This also implies that the dominant balance is of advection with buoyancy forces, which, however, contradicts the evidence from plots of $V_i, i = 1, 2, 3$ (see above).

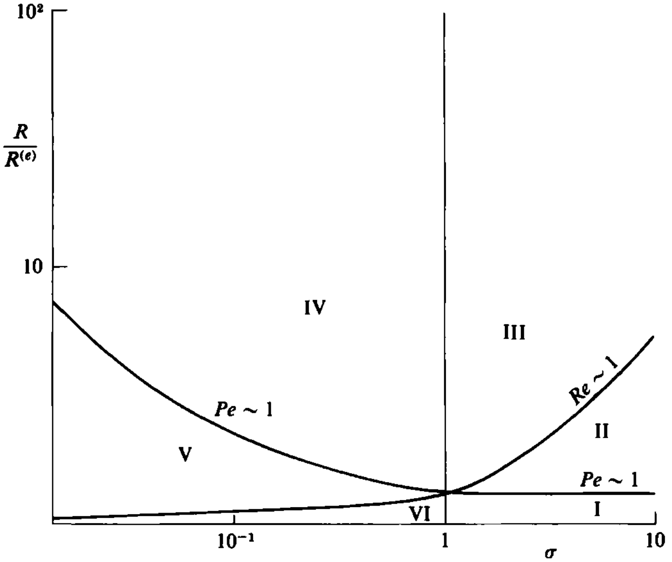

FIGURE 12. Different regimes of convection (after JMW). The $(R, \sigma)$-plane is divided schematically into regions bounded by lines on which the Péclet number, the Reynolds number or the Prandtl number is of order unity.

### 5.3. *Further studies of* $\sigma < 1$

In an attempt to clarify the above $N$- and $Re$-scalings, three further series of runs were made, two at fixed $R = 2000$ and $3500$, and one where $R$ was varied with $\sigma = 0.1$. The latter set is interesting because the output indicates $N \approx 1$ for $R = 2000$, suggesting that as in MW and JMW there is a second critical Rayleigh number $R^*$ below which convective heat transport is negligible and the simple expansion and model of §2.2 are valid. We are primarily interested in the asymptotic scaling of $R$ with $Re$, since $Re \propto R^{\frac{1}{2}}$ to be consistent with the reduced free-fall convection hypothesis. Just as at $\sigma = 1$, $\mathrm{d} \ln N / \mathrm{d} \ln R$ is still changing significantly for $R < 10000$ (to which accuracy considerations restrict us when $\sigma = 0.1$), and it is therefore no surprise that unfortunately $Re(R)$ is also far from a power-law dependence. The detailed properties of $\boldsymbol{u}$ and $T$ vary with $R$ much as for $\sigma = 1$.

The additional runs with $\sigma < 1$ help a little to resolve the issues raised in §5.2. Figure 11 (*a*) is the customary graph of the heat flux $N$ on log–log paper. None of the plots made for different values of $R$ is by itself particularly convincing, but taken together they suggest $\mathrm{d} \ln N / \mathrm{d} \ln \sigma \approx 0.2$–$0.3$, provided $N$ is not too close to unity. Figure 11 (*b*) shows smaller $N$ satisfy $N - 1 \propto \sigma^e$ where $e \approx 1$–$1.2$. Sadly for the durability of these scalings, figure 13 (*b*) shows that $N \propto \ln \sigma$ is just as good a fit to the computed heat fluxes at $R = 5000$. Nevertheless, the power laws change where $Pe \approx 7$, which is a low, but not implausible, value at which to expect properties of the convection to alter. Similarly, irrespective of $R$ and $\sigma < 1$, at $Pe \approx 10$ the vorticity-generation term $V_2$ becomes maximal in the spiral attracting regions of flow rather than in the centres of the cube faces.

Otherwise there is surprisingly little change in the convection at this $Pe$, apparently because the advective and dissipative terms still dominate the vorticity equation even when $R = 2000$. There are few surprises in the forms of the fields themselves. A gradual variation in $V_i$ and $T_i$ becomes pronounced when $Re \approx 150$: $T_2$ falls to approximately $0.4T_4$, the profiles $T_i(z)$ become less rounded to resemble those of figure 10(*c*), and the maxima of $V_t$ and $V_3$ lie exterior to (respectively to one side of and below) the spiral attractors (although this is not an invariable rule). However, there is no corresponding change in the heat-flux scalings, so the significance of this is unclear.

Our results for $\sigma < 1$ are best summarized with reference to the regime diagram of figure 12. (Regions I, II and III with $\sigma > 1$ are included by analogy with JMW.) In IV, where advection dominates, we have tentatively shown $N \propto \sigma^{0.2-0.3}$ and that convection takes place at the reduced free-fall velocity so $Re \propto \sigma^{-0.5}$. Region V is enlarged compared to JMW; because of the absence of 'flywheel' solutions we have to go to higher $R$ to achieve the same $Pe \sim 1$ that divides IV and V. Here $N-1 \propto \sigma^{1-1.2}$, and $Re$ depends more weakly on $\sigma$. Lastly, VI corresponds to $Re$ and $Pe \ll 1$, where we expect the results of §2.2 to apply so that $N-1 \propto \sigma^2$ and $Re$ is independent of $\sigma$. There appears to be a discontinuity in the heat-flux gradient as a function of $R$ as the boundary between VI and V is crossed, although we have not been able to study this as closely as JMW.

## 6. Variation of initial conditions and stability

This section goes further than §3.2 into the effect of changing the initial conditions. First we introduce the notation CH/I (for Chandrasekhar 1961) to describe the (1, 1, 1)-mode velocity perturbation used in §§4 and 5, and R2/I for the developed $l = 1$ convection which results. (Note that because of the symmetries involved it would be better to take $2^{-\frac{1}{2}}l$ as a measure of wavelength.) To study convection with $l = 2^{\frac{1}{2}}$ we employ as initial perturbation the pattern CH/R, derived from CH/I by the transformation $x+y \rightarrow x$, $x-y \rightarrow y$, giving an $F(\boldsymbol{x}) = (\cos \pi x + \cos \pi y) \sin \pi z$.

Three runs were made with this $F$ and $\sigma = 1$, at $R = 5$, 10 and $20 \times 10^3$. Near the end of each, a three-dimensional solution became unstable. We can estimate from measures of the flow, e.g. $u_{xm}$, the maximum value of $|u_x|$, that solutions R2/R are approached and the flow approximates them for 20–30 $t_0$, where $t_0 = 1/u_{zm}$ is the turnover time. As we would expect, since the fluid is incompressible, the maximum values of $|\boldsymbol{u}|$ now lie on the planes $z = 0$ and 1, rather than on vertical edges of the cube. When the instability develops $u_{xm}/u_{zm}$ falls by 90% in a few $t_0$, apparently leading to an $x$-independent solution. Runs at $R = 5000$, $\sigma = 0.05$ and 10 were not integrated for so many $t_0$. Although the computed $N$ are higher than those of R2/I, the value is not settling down in the same way, suggesting that instability will also occur. Convection with $l = 2^{-\frac{1}{2}}$ may be studied similarly: one run was made at $R = 20000$, $\sigma = 1$, and an unstable solution was found with $N$ less than the corresponding values for R2/R and R2/I. The timescale for the instability to appear is apparently related to that of the full development of (unstable) structures where viscosity is locally negligible: for R2/I this growth of other modes is prevented by the boundary conditions (§2.3).

Figure 13(*a*) gives the impression that, as a function of $R$, the heat transport by each square planform with $l \lesssim 1$ slackens off after an initial steep rise to an $N$ close to the maximum for rolls, with $\mathrm{d} \ln N / \mathrm{d} \ln R$ decreasing as $R \rightarrow \infty$. This implies that for $\sigma = 1$ the maximum $N(R)$ for rolls is an envelope function of $N(R, l)$ for all square-planform wavelengths $l$. This helps to explain why the numerically determined heat transport by rolls agrees with experimental results for $\sigma \approx 1$ where the flow is three-dimensional and turbulent (Busse 1978).

The next velocity pattern to study was suggested by numerical integration of (2.3)

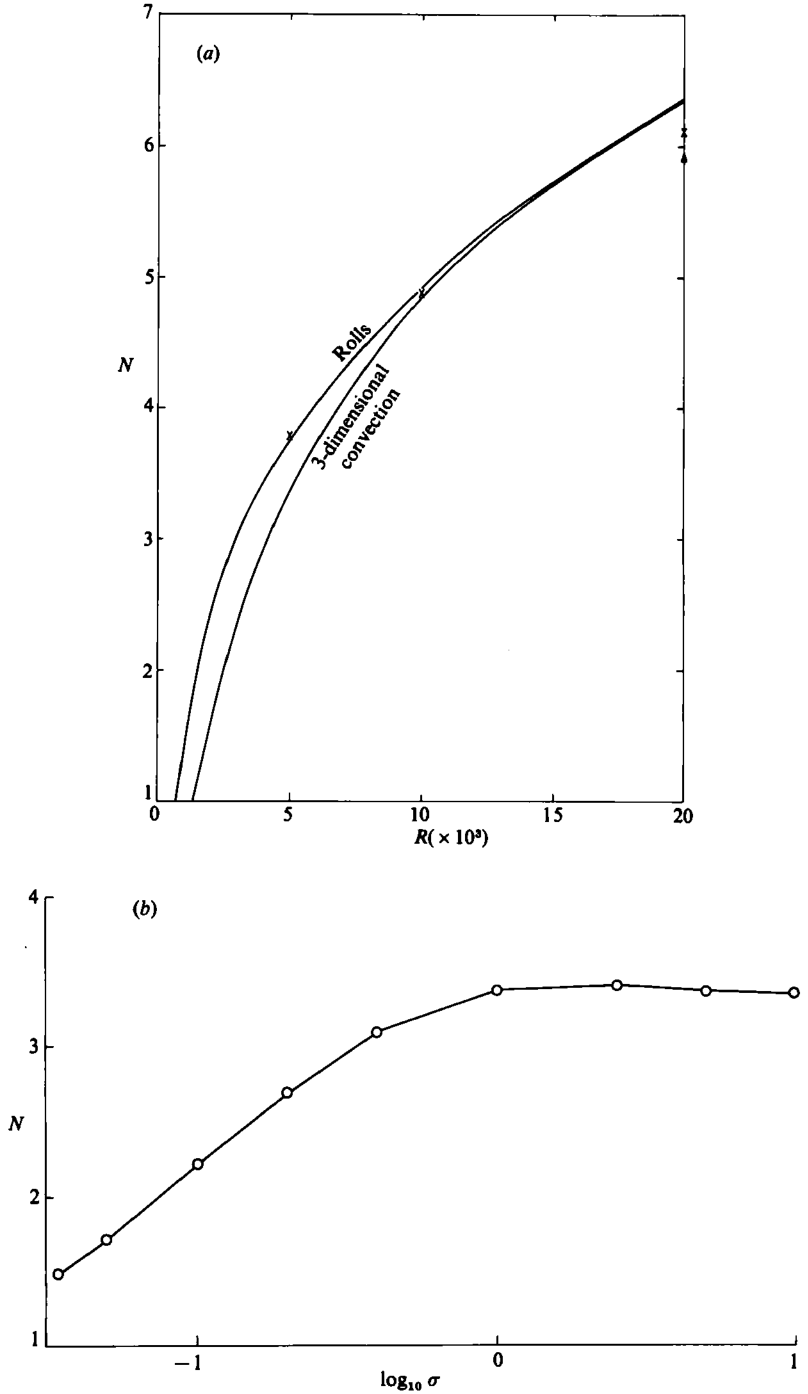

FIGURE 13. Nusselt number $N$ plotted ($a$) as a function of Rayleigh number $R$, for $\sigma = 1$, and ($b$) as a function of Prandtl number $\sigma$ for $R = 5000$. In ($a$) the upper line is $N$ for rolls; the points marked × are for the unstable solutions with wavelength $l = 2^{\frac{1}{2}}$ and △ is for a solution $l = 2^{-\frac{1}{2}}$.

as $\sigma$ and $r < r^{(f)}$ were varied, using many different initial conditions. If $b = f \gg a, d$ and $e$ initially, there was a violent transient, followed by $b$ and $f$ falling to zero. Only on a timescale long compared with those naturally occurring in (2.3) did the motion recover. We were able to duplicate this behaviour to a very limited extent for $R = 5000$ and $\sigma = 1$; by taking $b = 10a$ flow was reduced for an interval of $\approx t_0$. When an initial (2, 0, 2) temperature perturbation was included, the heat-transport reduction lasted for a slightly shorter time. Here $t_0$ is based on the initial $u_{zm}$, which is about half the ultimate equilibrium value. In (2.3) this 'mode suppression' arises apparently because the higher-order mode is linearly stable if $r < r^{(f)}$, and acts as a sink for 'energy' in the (1, 1, 1). The remaining results from solving (2.3) were entirely predictable, and we conclude that it is unnecessary to carry out other fully three-dimensional calculations starting with initial conditions of (1, 1, 1) and (2, 0, 2) form.

We now take as initial velocity pattern DY/I, derived from the flow DY of paper A, so that

$$F(\boldsymbol{x}) = (\cos \pi x \cos \pi y + \tfrac{1}{8}[\cos 2\pi x + \cos 2\pi y]) \sin \pi z.$$

It is topologically different (as discussed in §1) from CH/I and related patterns. However, motion with the topologically similar hexagonal planform is unstable near onset, unless the density $\rho$ has a quadratic dependence on $T$ (Busse 1967). As expected, a run started with DY/I at $R = 10000$, $\sigma = 1$ led to R2/I. Two runs were then made with an initial large-amplitude DY/I perturbation, setting

$$\rho = \rho_0(1 - \beta^*[T - T_0]^2),$$

but the resulting flows were nevertheless topologically equivalent to R2/I. (The appropriately redefined $R$ were 40 and $18 \times 10^3$, $\sigma = 1$ and 5.) It seems the shape and small extent of the computational box is the dominant factor. Moreover, it is not easy to discover which problems, subject also to the constraint described in §3.2, lead to a changed topology of $\boldsymbol{u}$. Consequently no more work was carried out in this direction.

With $\rho$ once more linearly dependent on $T$, runs were started without any flow by using temperature perturbations. Two were tried:

$$\theta_1 = (1-z) + \frac{1}{20} \sum_{\substack{m,n=1 \\ m \geqslant n}}^{5} \cos n\pi x \cos m\pi y \sin \pi z$$

and

$$\theta_2 = (1-z) + \frac{1}{20}\left( \sum_{\substack{m,n=1 \\ m \geqslant n}}^{4} \cos n\pi x \cos m\pi y \sin \pi z + \sum_{m=1}^{4} \cos m\pi y \sin \pi z \right).$$

The factor $\frac{1}{20}$ is after Grötzbach (1982). $\theta_1$ was used at $R = 5000$, $\sigma = 0.05$ and $\sigma = 10$, and each solution was apparently tending to R2/I when the runs were terminated. Inclusion of the $x$-independent terms $\theta_2$ leads to rolls with predictable alignment, although these are slow to develop fully. For the run with $\sigma = 10$, $N$ undergoes a damped oscillation with period $3t_0$ as the variation in $x$ fades: but, after three periods, $u_{xm}/u_{zm}$ remains approximately 0.06 and $\omega_{zm}/u_{zm} \approx 10^{-2}$. There are also irregular, short-timescale $O(\frac{1}{5}t_0)$, small-amplitude excursions in $u_{ym}$ and $u_{zm}$. These are not found for $\sigma = 0.05$: instead $u_{xm}$ moves erratically and not always monotonically to about 0.6 % of $u_{zm}$ in a time $O(50t_0)$. $t_0$ is not precisely determined, because $u_{zm}$, $u_{ym}$ and $N$ are still monotonically increasing at the end of the run: we infer that 'flywheel' convection is developing and that ultimately $u_{xm} \rightarrow 0$.

Finally, a computation started using $\theta_2$ at $R = 30000$, $\sigma = 1$ unexpectedly led to roll-like motion with $u_{ym}$ small and erratically decreasing: $u_{ym}/u_{zm} \approx 3\,\%$ at time $50t_0$. This run is also remarkable for an irregular, small-amplitude ($\Delta N \approx 0.03$), small-timescale $O(5t_0)$ variation in $N$, which moreover is uncorrelated with similar changes in $u_{xm}$ and $u_{zm}$.

In all of the runs employing $\theta_2$, the variation in the direction of the 'roll' axis has a wavelength equal to unity. This feature's persistence suggests it is a form of bimodal convection (Frick *et al.* 1983). Frick *et al.*, working at infinite Prandtl number with fixed-plate boundaries, show that square-pattern convection (R2 in our notation) is unstable to long-wavelength perturbations, which, however, have very slow growth rates. Bimodal convection would be expected to develop both at large $\sigma$, and for $\sigma = O(1)$, $R = O(20000)$ (Busse 1978). Rolls are unstable at small $\sigma$ (Busse 1972; Zippelius & Siggia 1982). However, all our computations show that R2/R is unstable and rolls are the outcome.

This result is explained by the small aspect ratio of the computational box, since wavelengths greater than it (except for the infinite one) cannot be represented by it (Grötzbach 1983). Thus the analytically favoured bimodal solutions, which typically have one horizontal wavelength much greater than the other, are excluded. We conclude that the absence of $x$- or $y$-independent perturbations is a necessary condition for R2/I or R2/R to develop, and that both, considered as part of a wider convective layer, are unstable to longer-wavelength disturbances.

## 7. Conclusion

We have studied in great detail a particular form of three-dimensional convection, principally by numerical calculation. Of our new results, perhaps the most interesting is the $(N, \sigma)$-scaling at constant $R$ for $\sigma < 1$, viz $N \propto \sigma^{0.2-0.3}$ when the Péclet number $Pe \gtrsim O(1)$, and $N-1 \propto \sigma$ for small $Pe$. JMW inferred on the basis of axisymmetric calculations that $N$ should be independent of $\sigma$ in three-dimensional convection: the difference arises because vorticity transport is significant in a square cell. However, like JMW we find that the $Re = 1$ and $Pe = 1$ lines divide parameter space into regions with different physical properties. It is remarkable too how $Re$ and $Pe$ determine the forms of $\boldsymbol{\omega}$ and $T$ almost independently of one another. Moreover, the steep gradients of $\boldsymbol{\omega}$ which occur for $Re$ large are greater than in two-dimensional computations.

We have not found any statistically steady, irregularly time-dependent solutions. Those that we produced by some of our choices of initial conditions in §6 were all apparently transient. We might infer that longer-wavelength motions are important for convective turbulence to develop from a pattern of square cells.

We have confirmed that the Boussinesq equations have solutions $\boldsymbol{u}$ with ergodic streamlines, as predicted by the truncated model (Arter 1983*b*). Owing to the relation between the streamline equations and second-order Hamiltonian systems, we should expect such behaviour to be generic, and it is therefore somewhat surprising that no experimental evidence for the phenomenon is available: Ozoe, Sato & Churchill (1979) demonstrate the converse. The value of a scan of $(R, \sigma)$-space such as ours is that it demonstrates that the key parameter is $Re$, and $Re \geqslant Re_c \gtrsim O(10)$ for ergodicity (and also the vertical component of vorticity $\omega_z$) to be significant. Doubtless geometry is a factor in determining $Re_c$, and the boundary conditions used by Ozoe *et al.* are different from ours, but since they, like most experimenters, are working with high-$\sigma$ fluids, it seems they are not at sufficiently large $Re$.

It is remarkable that ergodicity leads to no other new effects. We should expect a region occupied by ergodic flow to be isothermal at high $Pe$, except in boundary layers, where necessarily $\boldsymbol{u} \cdot \operatorname{grad} T \neq 0$, but we could have anticipated this type of solution from two-dimensional calculations. Note that even the initial dispersal of a blob of dye in a turbulent fluid, where we might expect ergodicity to be an important effect, may be described without explicit introduction of the concept (Garrett 1983).

In relation to fluid turbulence, it seems that ergodicity must be regarded as an epiphenomenon. There does, however, remain the possibility that it may lead directly to turbulence (B. McNamara, private communication). An ergodic flow undergoes a much greater degree of local shear than one where streamlines are closed (Arnold 1972): it is possible that this prevents, in a way that is hard to make precise, the atoms and molecules coming into full thermal equilibrium, i.e. the continuum hypothesis breaks down. In support of this is the correlation between ergodicity and Reynolds number: *Re* is a critical parameter in determining the onset of convective turbulence (Busse 1978). However, in agreement with the widely accepted view, McLaughlin & Orszag (1982) show that the Boussinesq equations are adequate to describe onset. Nonetheless, the experimental demonstration of an ergodic, laminar flow gains in importance.

Ergodicity should not overshadow another curious discovery, namely that, in laminar convection, vertical lines may be drawn through the flow where the isotherms do not have a boundary-layer structure near either the top or the bottom. Presumably the resulting local inefficiency in the heat transport is compensated for by changes in the velocity field due to the increased buoyancy force associated with these regions.

Like most of the preceding results, it is not clear how this last one applies to astrophysical convection, as we have failed to produce flows with the observed topological form. Introducing other asymmetries into the system of equations may help, but our results are not very encouraging (§6), and understanding these new effects may not in any case be straightforward. We shall have to study other planforms to be certain in particular that the heat transport is a strong function of $\sigma < 1$; this does, however, seem likely, since the results of MW and JMW that $N$ is independent of $\sigma < 1$ are in conflict with mixing-length theories of stellar convection (Gough 1977).

I wish to thank Dr N. O. Weiss especially for encouraging me to proceed with the numerical calculations: Dr B. McNamara provided valuable advice on Hamiltonian dynamics. I am very grateful for the programming assistance given by Dr S. Davies of DAPSU, Queen Mary College, London, and for the help provided by DAPSU, QMC Computer Centre, and Drs R. Stratford and R. D. Harding of Cambridge University. The SERC provided both a studentship and time on the DAP. The output of the DAP runs was analysed on the IBM 370/165 and IBM 3081 of the Cambridge University Computing Service.

## Appendix

Below are the parameters for nearly all the runs made: $l = 1$ unless otherwise stated. In brackets are the corresponding Nusselt number $N$ (in boldface) and Reynolds number *Re* (Péclet number $Pe = \sigma\, Re$). Single numbers in brackets are $N$ for rolls: if starred they were derived using the IBM 3081 of the Cambridge University Computing Service on a mesh of 24 × 24 (single star) or 48 × 48 (double star) points, with a code described by Moore *et al.* (1973).

$\sigma = 0.1$

$R = 2000$ (**1.16**, 54), $R = 2500$ (**1.34**, 79), $R = 3000$ (**1.53**, 103), $R = 3500$ (**1.73**, 126), $R = 5000$ (**2.22**, 184), $R = 7500$ (**2.79**, 259), $R = 10000$ (**3.21**, 320).

$\sigma = 1$

$R = 1500$ (**1.19**, 7.1), 2000 (**1.66**, 14.2), 2500 (**2.82***), 3500 (**2.68**, 26.8), 4000 (**3.45**), 5000 (**3.39**, 35.9), (**3.77**), 7500 (**4.41**), 10000 (**4.85**, 58.5) (**4.91***), 15000 (**5.70**, 76.4) (**5.72***), 20000 (**6.31**, 92.1) (**6.35***), 25000 (**6.80**, 106) (**6.88***), (**7.02****), 30000 (**7.20**, 119), 35000 (**7.55**, 131), 40000 (**7.86**, 143), 60000 (**8.86**, 183).

$R = 2000$

$\sigma = 0.05$ (**1.07**, 65), $\sigma = 0.1$ (**1.16**, 54), $\sigma = 0.2$ (**1.33**, 41), $\sigma = 0.4$ (**1.51**, 28).

$R = 3500$

$\sigma = 0.02$ (**1.12**, 245), $\sigma = 0.035$ (**1.26**, 203), $\sigma = 0.05$ (**1.39**, 179), $\sigma = 0.1$ (**1.73**, 126), $\sigma = 0.2$ (**2.09**, 82), $\sigma = 0.4$ (**2.43**, 52).

$R = 5000$

$\sigma = 0.035$ (**1.50**, 317), 0.05 (**1.71**, 269), 0.07 (**1.95**, 226), 0.1 (**2.22**, 184), 0.2 (**2.70**, 116), 0.4 (**3.10**, 70.2), 1 (**3.39**, 35.9), 2 (**3.42**, 20.6), 5 (**3.38**, 8.96), 10 (**3.37**, 4.56).

$l = 2^{\frac{1}{2}}$, $\sigma = 1$ (unstable)

$R = 5000$ (**3.79**, 38.7), 10000 (**4.88**, 63.6), 20000 (**6.12**, 103).

$l = 2^{\frac{1}{2}}$, $R = 5000$ (unstable?)

$\sigma = 0.05$ (**2.7**, 420), $\sigma = 10$ (**4.0**, 5.8).

$l = 2^{-\frac{1}{2}}$, $\sigma = 1$ (unstable)

$R = 20000$ (**5.91**, 80.2).

$l = 1$, density quadratically dependence on temperature

$\sigma = 1$, $R = 40000$ (**4.73**, 64.8). $\sigma = 5$, $R = 18000$ (**3.1**, 10).

## REFERENCES

Ahlers, G. & Behringer, R. P. 1978 Evidence of turbulence from the Rayleigh–Bénard instability. *Phys. Rev. Lett.* **40**, 712–715.

Arnold, V. 1966 Sur la géométrie différentielle des groups de Lie de dimension infinie et ses applications à l'hydrodynamique des fluides parfaits. *Ann. Inst. Fourier Grenoble* **16**, 319–361.

Arnold, V. I. 1972 Notes on the three-dimensional flow pattern of a perfect fluid in the presence of a small perturbation of the initial velocity field. *Prikl. Mat. Mekh.* **36**, 255–262 [English transl. *Appl. Math. Mech.* **36**, 236–242].

Arter, W. 1982 Convective motions in an imposed horizontal magnetic field. PhD thesis, University of Cambridge.

Arter, W. 1983*a* Magnetic flux transport by a convecting layer – topological, geometrical and compressible phenomena. *J. Fluid Mech.* **132**, 25–48.

Arter, W. 1983*b* Ergodic stream-lines in steady convection. *Phys. Lett* **97 A**, 171–174.

Arter, W. 1984*a* Magnetic flux transport by a convecting layer including dynamical effects. *Geophys. Astrophys. Fluid Dyn.* (in press).

BUSSE, F. H. 1967 The stability of finite amplitude cellular convection and its relation to an extremum principle. *J. Fluid Mech.* **30**, 625–649.

BUSSE, F. H. 1972 The oscillatory instability of convection rolls in a low Prandtl number fluid. *J. Fluid Mech.* **52**, 97–112.

BUSSE, F. H. 1978 Non-linear properties of thermal convection. *Rep. Prog. Phys.* **41**, 1929–1967.

CHANDRASEKHAR, S. 1961 *Hydrodynamic and Hydromagnetic Stability*. Clarendon.

COOLEY, J. W., LEWIS, P. A. W. & WELCH, P. D. 1970 The fast Fourier transform algorithm: programming considerations in the calculation of sine, cosine and Laplace transforms. *J. Sound Vib.* **12**, 315–337.

CROSS, M. C. 1982 Ingredients of a theory of convective textures close to onset. *Phys. Rev.* **A 25**, 1065–1076.

CROSS, M. C. 1983 Phase dynamics of convective rolls. *Phys. Rev.* **A 26**, 490–498.

CROSS, M. C., DANIELS, P. G., HOHENBERG, P. C. & SIGGIA, E. D. 1983 Phase-winding solutions in a finite container above the convective threshold. *J. Fluid Mech.* **127**, 155–183.

DEARDORFF, J. W. & WILLIS, G. E. 1967 Investigation of turbulent thermal convection between horizontal plates. *J. Fluid Mech.* **28**, 675–704.

DROBYSHEVSKI, E. M. & YUFEREV, V. S. 1974 Topological pumping of magnetic flux by three-dimensional convection. *J. Fluid Mech.* **65**, 33–44.

FRICK, H., BUSSE, F. H. & CLEVER, R. M. 1983 Steady three-dimensional convection at high Prandtl numbers. *J. Fluid Mech.* **127**, 141–153.

GARRETT, C. 1983 On the initial streakiness of a dispersing tracer in two- and three-dimensional turbulence. *Dyn. Atmos. Oceans* **7**, 265–277.

GOUGH, D. O. 1977 Stellar convection. In *Problems of Stellar Convection* (ed. E. A. Spiegel & J.-P. Zahn). Lecture Notes in Physics, vol. 71, pp. 349–363. Springer.

GREENSIDE, H. S., COUGHRAN, W. M. & SCHRYER, N. L. 1982 Nonlinear pattern formation near the onset of Rayleigh–Bénard convection. *Phys. Rev. Lett.* **49**, 726–729.

GRÖTZBACH, G. 1982 Direct numerical simulation of laminar and turbulent Bénard convection. *J. Fluid Mech.* **119**, 27–53.

GRÖTZBACH, G. 1983 Spatial resolution requirements for direct numerical simulation of Rayleigh–Bénard convection. *J. Comp. Phys.* **49**, 241–264.

HÉNON, M. 1966 Sur la topologie des lignes de courant dans un case particulier. *C. R. Acad. Sci. Paris* **A 262**, 312–314.

HOCKNEY, R. W. & JESSHOPE, C. R. 1981 *Parallel Computers*. Adam Hilger.

JENKINS, D. R. & PROCTOR, M. R. E. 1984 The transition from roll to square-cell solutions in Rayleigh–Bénard convection. *J. Fluid Mech.* **139**, 461–471.

JHAVERI, B. & HOMSY, G. M. 1980 Randomly forced Rayleigh–Bénard convection. *J. Fluid Mech.* **98**, 329–348.

JONES, C. A., MOORE, D. R. & WEISS, N. O. 1976 Axisymmetric convection in a cylinder. *J. Fluid Mech.* **73**, 353–388.

KRISHNAMURTI, R. 1970 On the transition to turbulent convection. Part 1. The transition from two- to three-dimensional flow. *J. Fluid Mech.* **42**, 295–307.

KRISHNAMURTI, R. 1973 Some further studies on the transition to turbulent convection. *J. Fluid Mech.* **60**, 285–303.

LIPPS, F. B. 1976 Numerical simulation of three-dimensional Bénard convection in air. *J. Fluid Mech.* **75**, 113–148.

LIPPS, F. B. & SOMERVILLE, R. C. J. 1971 Dynamics of variable wavelength in finite-amplitude Bénard convection. *Phys. Fluids* **14**, 759–765.

LORENZ, E. N. 1963 Deterministic nonperiodic flow. *J. Atmos. Sci.* **20**, 130–141.

MCLAUGHLIN, J. B. & ORSZAG, S. A. 1982 Transition from periodic to chaotic thermal convection. *J. Fluid Mech.* **122**, 123–142.

MALKUS, W. V. R. & VERONIS, G. 1958 Finite-amplitude cellular convection. *J. Fluid Mech.* **4**, 225–260.

MOORE, D. R. & WEISS, N. O. 1973 Two-dimensional Rayleigh–Bénard convection. *J. Fluid Mech.* **58**, 289–312.

MOORE, D. R., PECKOVER, R. S. & WEISS, N. O. 1973 Difference methods for time-dependent two-dimensional convection. *Comp. Phys. Commun.* **6**, 198–220.

ORSZAG, S. A. 1971 Numerical simulation of incompressible flows within simple boundaries. I. Galerkin (spectral) representations. *Stud. Appl. Maths* **50**, 293–327.

OZOE, H., YAMAMOTO, D., CHURCHILL, S. W. & SAYAMA, H. 1976 Three-dimensional numerical analysis of laminar natural convection in a confined fluid heated from below. *Trans. ASME* C: *J. Heat Transfer* **98**, 202–207.

OZOE, H., SATO, N. & CHURCHILL, S. 1979 Experimental confirmation of the three-dimensional streaklines previously computed for natural convection in inclined rectangular enclosures. *Intl Chem. Engng* **19**, 454–462.

PEYRET, R. & TAYLOR, T. D. 1983 *Computational Methods for Fluid Flow.* Springer.

RIAHI, N. 1981 Boundary-layer solutions of single-mode convection equations. *J. Fluid Mech.* **102**, 211–219.

ROBERTS, K. V. & WEISS, N. O. 1966 Convective difference schemes. *Math. Comp.* **20**, 272–299.

SCHLÜTER, A., LORTZ, D. & BUSSE, F. 1965 On the stability of steady finite amplitude convection. *J. Fluid Mech.* **23**, 129–144.

STUART, J. T. 1964 On the cellular patterns in thermal convection. *J. Fluid Mech.* **18**, 481–498.

TOOMRE, J., GOUGH, D. O. & SPIEGEL, E. A. 1982 Solutions of multimode convection equations. *J. Fluid Mech.* **125**, 99–122.

VELTISHCHEV, N. F. & ZELNIN, A. A. 1975 Numerical solution of cellular convection in air. *J. Fluid Mech.* **68**, 353–368.

VERONIS, G. 1966 Large amplitude Bénard convection. *J. Fluid Mech.* **26**, 49–68.

WEISS, N. O. 1966 The expulsion of magnetic flux by eddies. *Proc. R. Soc. Lond.* A **293**, 310–328.

WHITEMAN, K. J. 1977 Invariants and stability in classical mechanics. *Rep. Prog. Phys.* **40**, 1033–1069.

ZIPPELIUS, A. & SIGGIA, E. D. 1982 Disappearance of stable convection between stress-free boundaries. *Phys. Rev.* **A 26**, 1788–1790.